Chapter 1

MIMO Radar Technology

Shunqiao Sun[1]

Automotive radar with a small number of antennas has been used for advanced driver-assistance systems (ADAS) purposes since the late of 1990s. These early automotive radars mostly provided target detection and velocity information. However, current generation of automotive radar for ADAS has rather limited ability to resolve closely spaced targets. LiDAR systems have better angular resolution (less than 1 degree) and have been introduced in Level 4 and Level 5 autonomous driving systems. LiDAR can provide point clouds. Via use of deep neural networks, such as PointNet [1] and PointNet++ [2], the point clouds can lead to target identification. However, due to its use of light spectrum wavelength, LiDAR is susceptible to bad weather conditions, such as fog, rain, snow and dust in the air. In addition, the cost of LiDAR is high. On the other hand, automotive radar with millimeter waveform technology has the potential to provide point clouds at much lower cost than LiDAR, and with more robustness to weather conditions. Such radar is referred to as a "high end radar," or *imaging radar* [3]. Computer vision techniques [1, 2] that were previously reserved for high resolution camera sensors and LiDAR systems, can be applied to imaging radar data to identify targets. For example, a car can be identified based on two-dimensional (2D) radar points of an imaging radar using PointNet [4]. Imaging radars have been attracting the interest of those developing fully autonomous vehicles, major Tier-1 suppliers, and automotive radar startups.

In addition to sensitivity, the important requirements for automotive radar are high resolution, low hardware cost and small size. Multiple-input multiple-output (MIMO) radar technology has been receiving considerable attention by the automotive radar community because it can achieve high angular resolution with relatively small numbers of antennas and receivers. For that ability, it has been exploited in current generation automotive radar for ADAS as well as in next generation high resolution imaging radar for autonomous driving. For autonomous driving, information in both azimuth and elevation is crucial. In particular, the height information of targets is required to enable drive-over and drive-under functions. Two typical scenarios are shown in Fig. 1.1. It is safe to drive over a metal beverage can on the road and to drive under a steel pedestrian bridge over the road. To meet such requirement, the array is required to have a large aperture in both azimuth and elevation. MIMO

[1] Department of Electrical and Computer Engineering, The University of Alabama, Tuscaloosa, AL, 35487

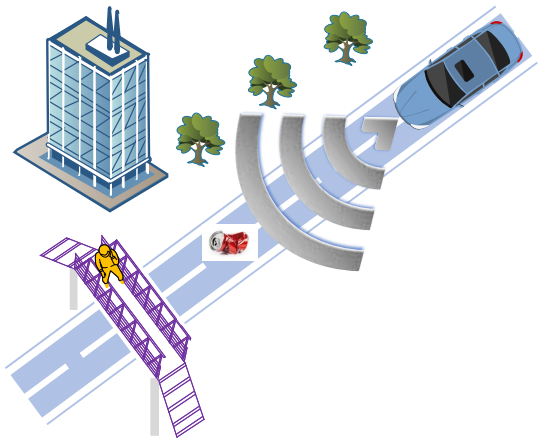

Figure 1.1 Automotive radars need to provide elevation resolution to enable drive-over and drive-under functions. © [2021] IEEE. Reprinted, with permission, from [5].

radar is a good candidate for high resolution imaging radar for autonomous driving. In MIMO radar the targets are first distinguished in range and Doppler domains. Then, large virtual arrays with hundreds of elements can be synthesized to provide high resolution in both azimuth and elevation. As a result, point clouds with similar performance as LiDAR can be generated at a much lower cost.

In this Chapter, we introduce the concept of imaging radars using MIMO technology, present some examples for synthesizing hundreds of virtual array elements by cascading multiple radar transceivers with each supporting a small number of antennas, and discuss design challenges.

1.1 Virtual Array Synthesis via MIMO Radar

In state-of-the-art automotive FMCW radar, the range and Doppler parameters of targets can be estimated by using single receive antenna. However, to estimate the angle parameter of targets, a receive antenna array is needed. In MIMO radar, the antennas transmit waveforms in a way that guarantees their orthogonality. At each receive antenna, the contribution of each transmit antenna is extracted by exploiting waveform orthogonality. For a uniform transmit antenna array with M_t transmit antennas and element spacing of d_t and a uniform receive antenna array with M_r receive antennas and element spacing of d_r, a virtual array with $M_t M_r$ elements can be synthesized. The array response of the *synthesized* array, i.e., the array corresponding to a MIMO radar can be expressed as $\mathbf{a}_t(\theta_t) \otimes \mathbf{a}_r(\theta_r)$. Here, $\otimes$ denotes the Kronecker product, and $\mathbf{a}_t(\theta_t)$ and $\mathbf{a}_r(\theta_r)$ are respectively the transmit and receive array steering vectors, corresponding to direction of departure (DOD) θ_t and direction of arrival (DOA) θ_r,

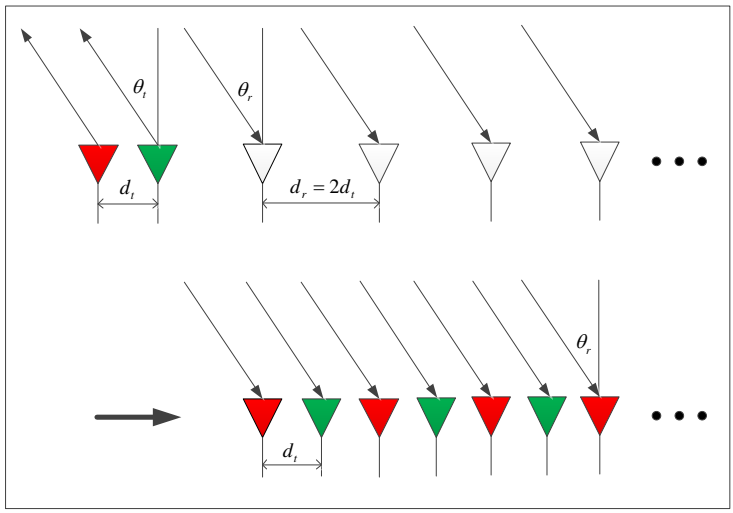

(a)

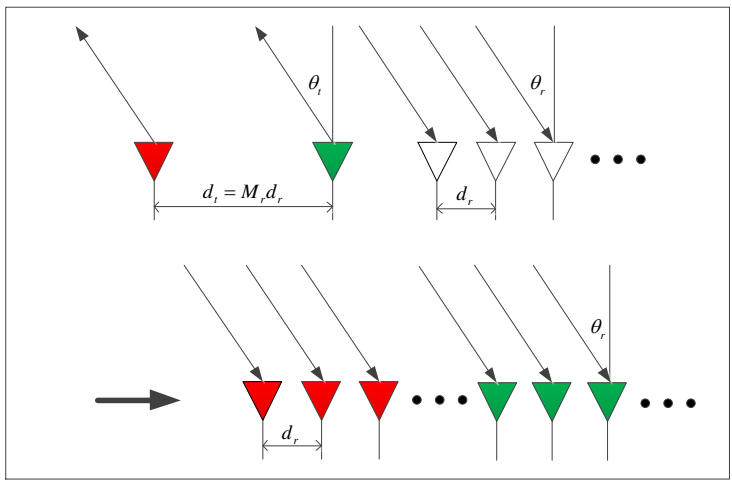

(b)

Figure 1.2 Illustration of different MIMO radar virtual array configurations using TDM or DDM scheme with $M_t = 2$ transmit antennas and M_r receive antennas: (a) interleaved with $d_r = 2d_t$ and $d_t = \frac{\lambda}{2}$; (b) stacked with $d_t = M_r d_r$ and $d_r = \frac{\lambda}{2}$. Different colors indicate the transmit antenna either transmits different time slots or codes. © [2020] IEEE. Reprinted, with permission, from [6].

defined below.

$$\mathbf{a}_t(\theta_t) = \left[1, e^{j2\pi\frac{d_t}{\lambda}\sin(\theta_t)}, \cdots, e^{j2\pi\frac{(M_t-1)d_t}{\lambda}\sin(\theta_t)}\right]^T, \tag{1.1}$$

$$\mathbf{a}_r(\theta_r) = \left[1, e^{j2\pi\frac{d_r}{\lambda}\sin(\theta_r)}, \cdots, e^{j2\pi\frac{(M_r-1)d_r}{\lambda}\sin(\theta_r)}\right]^T. \tag{1.2}$$

Figure 1.2 shows two MIMO radar configurations with $M_t = 2$ transmit and M_r receive antennas [6]. One is in interleaved mode with $d_r = 2d_t$ and $d_t = \frac{\lambda}{2}$ and the other is in stacked mode with $d_t = M_r d_r$ and $d_r = \frac{\lambda}{2}$. Here, $\lambda = \frac{c}{f_c}$ is the wavelength. It can be verified that for the both array configurations, the synthetic virtual arrays are equivalent to uniform linear arrays (ULAs) with $M_t M_r$ elements and spacing of d_r when $\theta_t = \theta_r$.

It should be noted that because MIMO radar transmits orthogonality waveform, when isotropic array elements are used, the array beampattern - also referred to as the MIMO radar array factor - is omnidirectional. Thus, MIMO radar loses the coherent array processing gain advantage enjoyed by traditional phased-array radar systems, which is $10\log N$ for a phased-array with N elements [7]; the SNR of the array response at a given angular direction is less than that of phased-array radar with transmit beamforming. Still, in the automotive application scenario, the high resolution angle finding ability of MIMO radar coupled with its low cost are viewed as more important than the loss of coherent processing gain.

1.2 Waveform Orthogonality Strategies in Automotive MIMO Radar

Virtual array synthesis in automotive radar using MIMO radar technology relies on the separability of the transmit signals of the different antennas. The separation is easier when the transmit signals of different antennas are orthogonal. In the following, we review techniques to achieve waveform orthogonality while transmitting FMCW, such as time division multiplexing (TDM), Doppler division multiplexing (DDM) and frequency division multiplexing (FDM).

1.2.1 Waveform orthogonality via time division multiplexing (TDM)

In TDM MIMO radar [8, 9, 10, 11, 12], only one transmit antenna is scheduled to transmit at each time slot. In Fig. 1.3, a signal processing example of a MIMO radar in TDM is given by NXP Semiconductors [13], where $M_t = 2$ transmit antennas emit FMCW chirps alternatively. The switch delay between transmit antennas is $\Delta t = T_{\text{PRI}}$. At each receive antenna, range FFTs of length N_r are conducted for each chirp and the FFT outputs of $2N_d$ chirps are assembled in two matrices corresponding to odd and even chirp sequences, respectively. The receive array corresponding to odd and even chirp sequences form two subarrays, which can be used to synthesize a virtual array according to interleaved or stacked configurations.

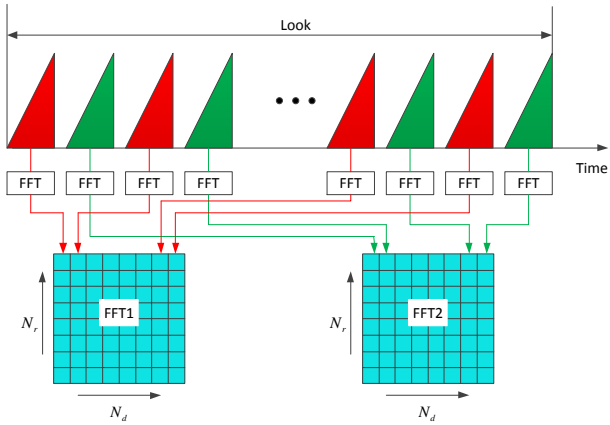

Figure 1.3 Example of radar signal processing with TDM scheme, where $M_t = 2$ transmit antennas transmit FMCW chirp sequences alternatively. The red and green color denote the odd and even echo chirp sequences, respectively. The range FFTs are conducted for each chirp and the FFT outputs are stored in two matrices corresponding to odd and even sequences, respectively for further processing. © [2020] IEEE. Reprinted, with permission, from [6].

For a moving target with velocity of v, the switching delays of transmit antennas introduce a target phase migration from chirp to chirp, which is defined as $\phi = 2\pi f_D \Delta t = \frac{4\pi}{\lambda} v\Delta t$. As a result, the virtual array pattern would be distorted [10]. In Fig. 1.3, the phase difference between corresponding columns in the two matrices is $\phi = \frac{4\pi}{\lambda} v T_{\text{PRI}}$. If $v = -0.5v_{\max}$ and $v = -v_{\max}$, where $v_{\max}$ is the maximum unambiguous detectable radial speed and $v_{\max} = \frac{c}{4f_c T_{\text{PRI}}}$, the phase shifts are $\phi = -\pi/2$ and $\phi = -\pi$, respectively. The array beampattern distortion is demonstrated in Fig. 1.4 for a moving target with range of 35m and azimuth angle of $\theta = 0^\circ$ [10]. Here, MIMO radar with $M_t = 2, M_r = 8$ operates in TDM fashion. As stated in [10], and can also be seen in Fig. 1.4, for interleaved MIMO array configuration, when the target velocity increases, the grating lobes at the edge of FOV show up, while the peak at the target direction decreases and totally disappears when $v = -v_{\max}$. For stacked MIMO array configuration, as the target velocity increases, the peak is slightly off the boresight with a mirror grating lobe at the opposite direction.

The phase migration introduced by every moving target in the virtual array response needs to be compensated for before angle finding. The phase shift estimate $\hat{\phi}$, can be obtained after each target velocity has been estimated based on the 2D-FFT of a single receive antenna, or non-coherent 2D-FFT integration of the same subarray. For example, in the example of Fig. 1.3, the phase in the beam vector of the subarray obtained from the even chirps needs to be compensated by multiplying them with

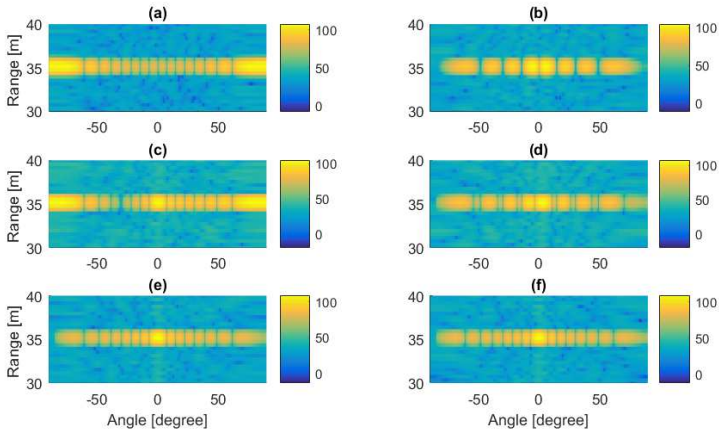

Figure 1.4 Examples of MIMO radar range and azimuth images using TDM with $M_t = 2, M_r = 8$ for a single target with range of 35m*, azimuth angle of $\theta = 0^\circ$. Two MIMO array configurations, interleaved (left column) and stacked (right column) are considered. The radial velocity of (a-b) $v = -v_{\max}$, (c-d) $v = -0.5v_{\max}$ and (e-f) $v = 0$. © [2020] IEEE. Reprinted, with permission, from [6].*

$e^{-j\hat{\phi}}$, while the phase in the beam vector of the subarray corresponding to odd chirps is kept unchanged.

It should be noted that, in TDM MIMO radar, the pulse repetition interval is enlarged by the transmit antenna number M_t. As a result, the maximum unambiguous detectable velocity will be reduced by a factor of M_t [14].

1.2.2 Waveform orthogonality via Doppler division multiplexing (DDM)

In one look, a total of N chirps (i.e., pulses) are transmitted sequentially, with pulse repetition interval T_{PRI}. All transmit antennas transmit simultaneously the same FMCW waveform, after multiplying it with a phase code that is different for each antenna, and changes between pulses, i.e., $x_m(n) = e^{j2\pi\alpha_m(n)}, m = 1, \cdots, M_t, n = 1, \cdots, N$ [15]. To separate the h-th transmit signal at the l-th receiver, after range FFT, a slow time Doppler demodulation is applied to all range bins corresponding to the same chirp. The Doppler demodulated outputs of N chirps are assembled into a vector $\mathbf{s}_l^h$. Then, the Doppler FFT is applied on the vector $\mathbf{s}_l^h$. To separate the transmit signals in the Doppler domain, one for the two methods described below can be applied.

The first approach is to design phase codes such that the Doppler FFT of the interference $e^{j2\pi(\alpha_m(n)-\alpha_h(n))}$ is shifted to a frequency that is higher than the maximum detectable Doppler frequency $f_D^{\max}$. Therefore, a LPF can be applied to remove the

interference [15]. One example of such phase codes is

$$\alpha_m(n) = \alpha_m n, m = 1, \ldots M_t, n = 1, \ldots N, \tag{1.3}$$

where the starting phase α_m is linear across different transmit antennas, i.e., $\alpha_m = a_0 m$. Figure 1.5 (a) shows the range and Doppler spectrum of a target with range of 75m and velocity of 10m/s. The automotive MIMO radar has two transmit antennas and transmit phase codes given in (1.3) with $a_0 = 1$ and $N = 512$. It can be seen that signals from different transmit antennas are shifted to higher Doppler spectrum, which can be removed via a LPF in Doppler domain. Under this approach, the radar pulse repetition frequency f_{PRF} should be larger than $M_t f_D^{\max}$ [16]. Thus, if the f_{PRF} is kept unchanged, the maximum detectable unambiguous Doppler frequency is reduced by a factor of M_t. In practice, a Doppler unfolding, or de-aliasing algorithm needs to be developed with different f_{PRF} in different looks.

The second approach is to design phase codes so that the Doppler FFT of the interference can be distributed into the entire Doppler spectrum as pseudo noise. It is desired to minimize the peak interference residual (PIR) in the Doppler spectrum [17] calculated using the discrete-time Fourier transform (DTFT) for $m = 1, \cdots, M_t$, i.e.,

$$\text{PIR} = \max_{f, m \neq h} \left| \sum_{n=1}^{N} e^{j2\pi(\alpha_m(n) - \alpha_h(n))} e^{j2\pi f n} \right|, \tag{1.4}$$

where $f \in \left[-\frac{1}{2} f_{\text{PRF}}, \frac{1}{2} f_{\text{PRF}}\right]$. Following equation (1.4), the cross-correlation of the spectra of two codes needs to be flat [17], since the Fourier transform of multiplication of two codes in the time domain is equivalent to convolution of spectrum of one code with time reversed and complex conjugate of the other. The maximum auto-correlation value of an unimodular sequence of length N is N. The ideal cross-correlation of two unimodular sequences of length N has magnitude of $\sqrt{N}$. Thus, in the ideal case, according to [17] the maximum power gain of the currently transmitted signal over other signals is $\sqrt{N}$. For example, the maximum achievable waveform attenuation is about 27.1dB for unimodular sequence set with $N = 512$.

Constant amplitude zero auto-correlation codes are good candidates for DDM. The discrete Fourier transform (DFT) of a constant amplitude zero auto-correlation code has also constant amplitude and zero auto correlation[18]. One of such examples is the Chu sequence [19], which is defined as $x_m(n) = e^{\frac{j\pi}{N} m(n+1)n}, m = 1, \ldots M_t, n = 1, \ldots, N$, where N is a prime number. In practice, the Chu sequence of prime length is first generated and then truncated into a length for efficient FFT. For example, we generate Chu codes of prime length 521 and truncate them to length $N = 512$. By calculation with FFT, the peak interference residual defined in (1.4) is $1.08\sqrt{N}$. Therefore, the waveform attenuation for Chu sequence of length $N = 512$ is about 26.4dB. In Fig. 1.5 (b), we show the range and Doppler spectrum of a target with range of 75m and velocity of 10m/s. The automotive radar has two transmit antennas and two Chu sequences of length $N = 512$ are applied for slow time DDM. It can be seen that the waveform attenuation is about 26dB.

In practice, binary phase codes are used due to hardware constraint [20]. The binary phase code sequences are obtained via exhaustive search such that the peak

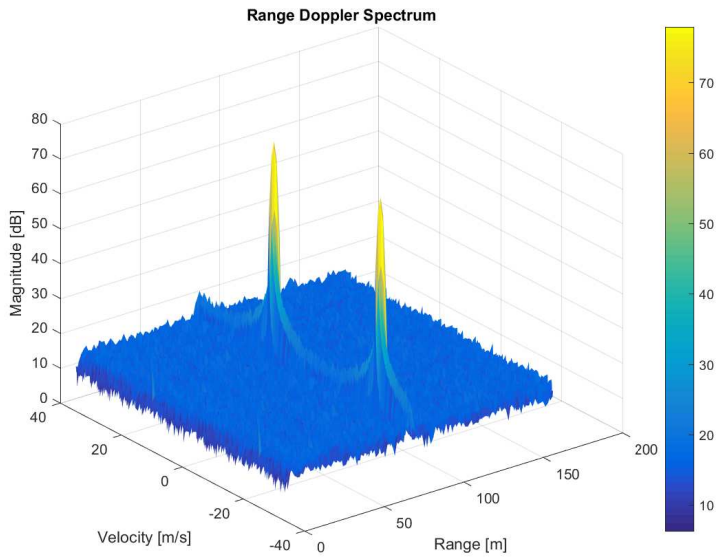

(a)

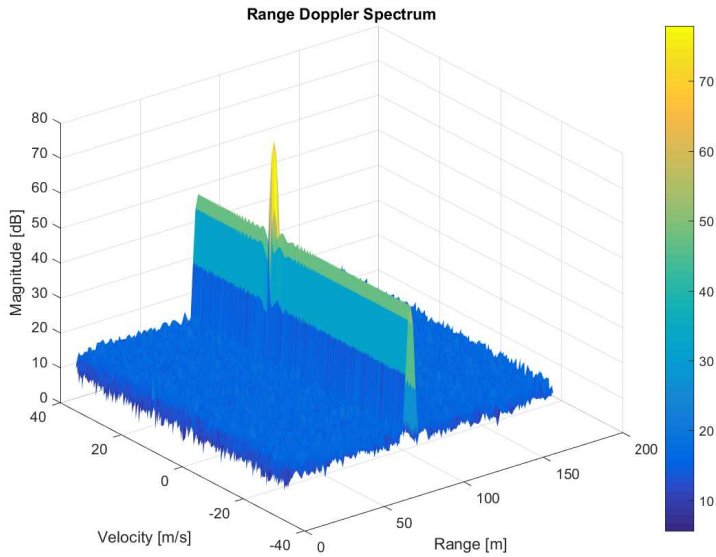

(b)

Figure 1.5 The range and Doppler spectra of a target with range of 75*m and velocity of* 10*m/s. The automotive MIMO radar has two transmit antennas and slow time phase coding of length* $N = 512$ *is applied for DDM. (a) phase shift codes defined in equation (1.3); (b) two Chu sequences. © [2020] IEEE. Reprinted, with permission, from [6].*

interference residual in (1.4) is low. As the code length increases, the search time will grow exponentially.

The benefit of slow time phase coding is that the interference from other transmitters does not affect different range bins. The range resolution is only determined by the bandwdith of FMCW chirp. Therefore, it avoids the range sidelobe issue using fast time phase coding. However, the Doppler sidelobes would be high due to the residual of the slow time phase coding. As a result, targets with low radar cross section (RCS), e.g., pedestrians, that are close to the target with strong reflections, e.g., trucks, might be masked by the waveform residual. In other words, the waveform residual reduces the radar dynamic range. Given the code length, the number of phase codes with good correlation properties is limited, or equivalently, the number of antennas that can transmit simultaneously is limited.

1.2.3 Waveform orthogonality via frequency division multiplexing (FDM)

In the FDM scheme, the transmitted signals are modulated by different carrier frequencies. According to [21], the separation of multiple transmit FMCW signals is achieved by shifting the m-th transmit FMCW chirp by an offset frequency $f_{\text{off},m}$. If the differences between all $f_{\text{off},m}$ are larger than twice of the cut-off frequency of the anti-aliasing BPF $f_b^{\max}$, which is determined by the maximum unambiguous detectable range and Doppler, the transmitted signals can be separated at the receive end. Specifically, the received signal at each receiver is first mixed with the same starting carrier frequency f_c. The separation of transmit signals in the mixer output can be implemented by a frequency shift followed by a low pass filter with cut-off frequency $f_b^{\max}$ [21]. Each receiver needs to carry out such frequency shift and filtering operation M_t times. As a result, high range resolution can be realized using a typical FMCW chirp with large bandwidth. Meanwhile, after FMCW demodulation, frequency shift and filtering operation, the FDM MIMO scheme can still utilize a low sampling rate determined by the beat signal.

Let us consider the FDM scheme in the context of the example in Section II, i.e., a FMCW LRR radar with maximum detectable range of 250 meters and maximum detectable velocity of 120 mph. For bandwidth $B = 150$ MHz and chirp duration $T = 50$ μs, the maximum beat frequency is $f_b^{\max} = f_R^{\max} + f_D^{\max} = 5.0274$ MHz. Therefore, the frequency shift for the m-th transmit antenna in the FDM scheme can be chosen as $f_{\text{off},m} = 12\,(m-1)$ MHz. The intermediate frequency (IF) should have a bandwidth of $12M_t$ MHz to hold the mixer output.

1.3 Angle Finding in Automotive MIMO Radar

In automotive MIMO radar with M_t transmit and M_r receive antennas, a virtual uniform linear array of M_tM_r elements can be synthesized with inter-element spacing d. The array response can be written as

$$\mathbf{y} = \mathbf{A}\,(\theta)\,\mathbf{s} + \mathbf{n}, \tag{1.5}$$

where $\mathbf{A}(\theta) = [\mathbf{a}(\theta_1), \cdots, \mathbf{a}(\theta_K)]$ is the virtual array steering matrix with

$$\mathbf{a}(\theta_k) = \left[1, e^{j\frac{2\pi}{\lambda}d\sin(\theta_k)}, \cdots, e^{j\frac{2\pi}{\lambda}(M_tM_r-1)d\sin(\theta_k)}\right]^T. \tag{1.6}$$

Here, $\mathbf{n}$ is a noise term and $\mathbf{s} = [\beta_1, \cdots, \beta_K]^T$, where β_k denotes the target reflection coefficient for the k-th target. The array response at a particular time instance consisting of data obtained at all the virtual receivers and corresponding to the same range-Doppler bin is defined as the *array snapshot*. In highly dynamic automotive scenarios, usually, only a small number of array snapshots, or even a single snapshot in the worst case is available [22].

In automotive MIMO radar with virtual ULA, angle finding can be done with digital beamforming (DBF) [23, 24, 25] by performing FFTs on snapshots taken across the array elements, , i.e., $\mathbf{y}$ in equation (1.16) (see Fig. 1.6). DBF can be implemented efficiently in an embedded DSP with a single snapshot. However, DBF is not a high resolution angle finding method. Higher resolution angle finding can be achieved with subspace based methods, such as MUSIC [26] and ESPRIT [27, 28, 29, 30], sparse sensing based methods [31, 32, 33, 34, 35, 36, 37, 38, 39], or the iterative adaptive approach (IAA) of [40] and [41]. The performance of subspace based angle finding methods relies on accurate estimation of the array covariance matrix with multiple snapshots, which is a challenging task in the highly non-stationary automotive radar scenarios. In such context, spatial smoothing [42] is applied for introducing virtual snapshots for array covariance matrix estimation. While sparse sensing based methods and IAA have high computational cost, they yield angle estimates based on a single snapshot, which is important for snapshot-limited automotive radar.

Achieving high angular resolution for L4 and L5 autonomous driving requirement using ULA with $d = \frac{\lambda}{2}$ is very expensive. According to [43], the 3dB beamwidth of antenna array with aperture size D is $\Delta\theta = 2\arcsin\left(\frac{1.4\lambda}{\pi D}\right)$. To achieve 3dB beamwidth of 1 degree, the antenna array aperture should be about $D \approx 51\lambda$. If the antenna array is ULA with inter-element spacing as half wavelength, it should be composed of about 100 array elements. Even with the help of MIMO radar technology, the cost of synthesizing such a large virtual ULA with half wavelength element spacing is very high. One way to further reduce the cost without sacrificing the high angular resolution is via the use of nonuniform, or sparse linear arrays (SLAs) [44, 45, 46, 47, 48, 49], synthesized with MIMO radar technology. In that context, selecting the locations of array elements and carrying out angle finding with the virtual sparse array are key problems.

1.3.1 High resolution angle finding with uniform linear array (ULA)

1.3.1.1 Subspace methods with spatial smoothing

The performance of subspace based angle finding methods requires an estimate of the array covariance matrix. Such estimate is typically obtained based on multiple snapshots. However, in highly dynamic automotive environment, it is not possible to obtain enough snapshots before the model of (1.16) changes. In such scenarios,

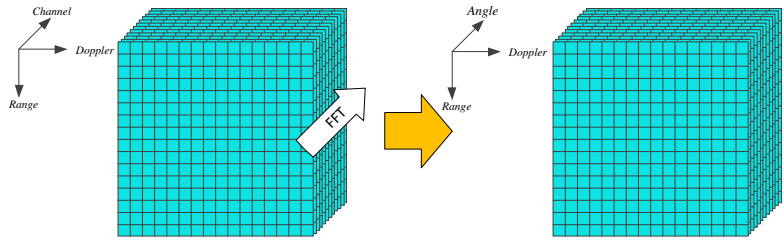

Figure 1.6 Digital beamforming (DBF). © [2020] IEEE. Reprinted, with permission, from [6].

spatial smoothing [42] can introduce virtual snapshots for array covariance matrix estimation. In spatial smoothing, the array snapshot, $\mathbf{y}$, is divided into overlapped sub-arrays of length L and a new sampled array covariance matrix $\mathbf{R} \in \mathbb{C}^{L \times L}$ is obtained based on the sub-array snapshots.

Eigenvalue decomposition of $\mathbf{R}$, along with the Akaike information criteria (AIC) metric [50], or the minimum description length (MDL) metric [51], can be used to identify the number of targets. It should be noted, however, that many ideal assumptions in the deduction of these criteria, including additive white Gaussian noise that is uncorrelated with source signal, and the availability of enough snapshots for an accurate covariance matrix estimation, might not be satisfied in practice. To this end, forward backward spatial smoothing techniques [52] have been widely applied to estimate the subarray covariance matrix for subspace methods based angle estimation. When the subarray length is shorter, more subarrays are available for covariance matrix calculation, and thus a more accurate subspace estimation would be expected. However, when subarray length is shorter, the DOA estimation resolution is reduced, so a tradeoff between obtaining the number of subarrays and length of subarray should be considered [53].

The target angles can be found by identifying the locations of peaks of the MUSIC pseudo spectrum [26], $P(\theta_i)$, computed at all possible θ_i's, i.e.,

$$P(\theta_i) = \frac{1}{\mathbf{a}_L^H(\theta_i)\mathbf{U}_\mathbf{n}\mathbf{U}_\mathbf{n}^H\mathbf{a}_L(\theta_i)}, \tag{1.7}$$

where $\mathbf{U}_\mathbf{n}$ is the noise subspace of $\mathbf{R}$ and $\mathbf{a}_L(\theta_i)$ is the array steering vector of length L corresponding to search direction θ_i. The computation cost of the MUSIC algorithm is high due to the angle search process. Alternatively, the ESPRIT algorithm could be used for angle estimation [27]. ESPRIT is also a subspace method, which exploits the array shift invariance properties, and has been widely used in practice. It has lower complexity than MUSIC, which, however, comes at the cost of reduced angular resolution. ESPRIT requires $2L$ sensors with $L > K$. To achieve the same angular resolution as MUSIC, ESPRIT needs twice as many sensors as MUSIC. As 2D arrays are needed in automotive radar in order to estimate both azimuth and elevation

angles, 2D ESPRIT algorithms [30] can be applied if the array element spacing is uniform rectangular.

1.3.1.2 Compressive sensing

MIMO radars equipped with millimeter wave technology offer wide bandwidth, thus achieving high range resolution. As a result, there are only a small number of targets that fall in the same range-Doppler bin, and thus, the targets are sparse in the DOA space. This property can be exploited by sparse sensing based high resolution methods for target angle estimation. To apply compressive sensing for DOA estimation, the whole DOA field of view is discretized into a fine grid. Assume that the DOA space is discretized on a fine grid with N points and there are K targets on the grid. The array response in (1.16) can be re-written as

$$\mathbf{y} = \mathbf{A}\mathbf{x} + \mathbf{n}, \tag{1.8}$$

where $\mathbf{A} = [\mathbf{a}(\theta_1), \cdots, \mathbf{a}(\theta_N)]$ is the basis matrix with $\mathbf{a}(\theta_i)$ denoting the array steering vector corresponding to the i-th grid point and $\mathbf{x} = [\beta_1, \beta_2, \cdots, \beta_N]^T$ is a sparse vector with K non-zero elements. The value of β_i is non-zero if there is a target at the i-th grid point. The coherence of the basis matrix, defined as

$$\mu \triangleq \max_{i \neq l} \frac{\left|\mathbf{a}^H(\theta_i)\,\mathbf{a}(\theta_l)\right|}{\|\mathbf{a}(\theta_i)\|_{\ell_2}\|\mathbf{a}(\theta_l)\|_{\ell_2}}. \tag{1.9}$$

needs to be low for obtaining uniform recovery guarantees [54]. When meeting the required coherence conditions, the DOA can be found by solving a ℓ_1 norm optimization problem, such as Dantzig selector [55] defined below

$$\begin{aligned} &\min \ \|\mathbf{x}\|_{\ell_1} \\ &\text{s.t.} \ \left\|\mathbf{A}^H(\mathbf{y} - \mathbf{A}\mathbf{x})\right\|_{\ell_\infty} < \eta. \end{aligned} \tag{1.10}$$

or greedy methods, such as orthogonal matching pursuit (OMP) [56].

In the above formulation, targets are assumed to be on the grid, which is not always possible in practice. While one can make the grid finer in order to capture the targets, the coherence of matrix $\mathbf{A}$ would increase, which would make the ℓ_1 norm solution invalid [57]. Thus, the performance of compressive sensing based methods is sensitive to targets appearing off the grid [58]. Sparse sensing and matrix completion based methods [38, 39] can avoid grid issues without sacrificing the high resolution performance.

1.3.1.3 Iterative adaptive approach (IAA)

The covariance matrix of M array snapshots $\mathbf{y}_l, l = 1, \cdots, M$, can be written as $\mathbf{R} = \mathbf{A}(\theta)\mathbf{P}\mathbf{A}^H(\theta)$, where $\mathbf{P}$ is a $K \times K$ diagonal matrix whose diagonal elements contains the power of target reflections. Angle finding in the IAA algorithm [40, 41] is carried out by iteratively estimating the reflection coefficient β_k. The estimate is

found by minimizing the weighted least square (WLS) cost function

$$\sum_{l=1}^{M} \|\mathbf{y}_l - \beta_k(l)\,\mathbf{a}(\theta_k)\|^2_{\mathbf{Q}^{-1}(\theta_k)}, \tag{1.11}$$

where $\|\mathbf{x}\|^2_{\mathbf{Q}^{-1}(\theta_k)} = \mathbf{x}^H \mathbf{Q}^{-1}(\theta_k)\,\mathbf{x}$ and the interference and noise covariance matrix $\mathbf{Q}(\theta_k) = \mathbf{R} - \hat{P}_k \mathbf{a}(\theta_k)\,\mathbf{a}^H(\theta_k)$. The solution is given by [40]

$$\hat{\beta}_k(l) = \frac{\mathbf{a}^H(\theta_k)\,\mathbf{R}^{-1}\mathbf{y}_l}{\mathbf{a}^H(\theta_k)\,\mathbf{R}^{-1}\mathbf{a}(\theta_k)}. \tag{1.12}$$

Then matrix $\mathbf{P}$ can be updated as $\hat{P}_k = \frac{1}{M}\sum_{l=1}^{M}\left|\hat{\beta}_k(l)\right|^2$. In IAA algorithm implementation, the DOA space is discretized into a fine grid of N points and steering matrix $\mathbf{A}$ is constructed in the same way as in compressive sensing. In addition, a standard delay and sum (DAS) beamformer is used to initialize $\mathbf{P}$,

$$\hat{P}_k = \frac{\sum_{l=1}^{M}\left|\mathbf{a}^H(\theta_k)\,\mathbf{y}_l\right|^2}{M\left|\mathbf{a}^H(\theta_k)\,\mathbf{a}(\theta_k)\right|^2}. \tag{1.13}$$

1.3.2 High resolution angle finding with sparse linear array (SLA)

As stated before, the cost of synthesizing a large virtual ULA of D elements with half wavelength element spacing is very high. One way to further reduce the cost without sacrificing the high angular resolution is via the use of nonuniform, or sparse linear arrays [59, 45, 44]. With MIMO radar technology, $M_t M_r < D$ virtual array elements can be synthesized. To make sparse linear array (SLA) aperture the same as the ULA, two virtual array elements should be deployed at the edge locations of the ULA. For the remaining virtual array elements, there are multiple possibilities to deploy. The main issue with SLA is that the grating lobes may introduce ambiguity in angle finding.

In automotive MIMO radar with virtual SLA, angle finding can still be done with conventional FFT or ESPRIT methods if the holes in the virtual SLA can be filled via interpolation or extrapolation techniques to mitigate the grating lobes [60, 61].

To mitigate the high sidelobes introduced by the sparse arrays, we utilize the matrix completion technology to interpolate/extrapolate the holes in the sparse arrays. Furthermore, matrix completion improves the SNR of array response as there is no loss/holes in the fully recovered arrays.

During one CPI of a typical automotive radar scenario, a dense point cloud with a high volume of targets could be detected in the range-Doppler spectrum [62]. The success of applying matrix completion in irregular one-dimensional (1D) or 2D sparse arrays relies on the following two facts:

F1) The number of targets in the same range-Doppler bin that need angle estimation is small since the targets are first separated in range-Doppler domain. In other

words, the targets are sparsely present in the angular domain and, as a result, the Hankel matrix constructed using the array response is low rank.

F2) The SNR in the array snapshot is much higher than that in the echo signal, since energy has been accumulated in both range and Doppler domains via the IDFT and DFT operations. The high SNR in the array snapshot help reduce the matrix completion error and improve the accuracy of angle estimation.

We will illustrate the array interpolation concept through matrix completion in one-dimensional sparse arrays and then extend it to two-dimensional sparse arrays.

1.3.2.1 One Dimensional Sparse Array Interpolation via Matrix Completion

Fig. 1.7 shows an example of the physical array configuration of an automotive radar which is a cascaded of 2 MIMO transceivers, where all transmit and receive antennas are clock synchronized. Let λ denote the wavelength of the carrier frequency. In this example, $M_t = 6$ transmit and $M_r = 8$ receive antennas are deployed on discretized grid points along the azimuth direction with an interval of length equal to 50λ. The interval is discretized uniformly with half-wavelength spacing. The transmit antennas transmit waveform in a way that, at each receive antenna, the contribution of each transmit antenna can be separated via DDM. Therefore, with MIMO radar technology, a virtual SLA with 48 array elements and aperture of 75λ is synthesized, as shown in Fig. 1.7. Compared to a ULA with half-wavelength interelement spacing and the same aperture, a high number of elements at certain locations are "missing" at the rednered virtual SLA (denoted by zeros in the virtual array of Fig. 1.7). However, the SLA approach uses only $M_t + M_r = 14$ physical antennas with significantly reduced mutual coupling effects [6].

Suppose an array snapshot contains K targets with DOAs θ_k, $k = 1, \cdots, K$. Without noise, the SLA response can be expressed as

$$\mathbf{y}_S = \mathbf{A}_S \mathbf{s}, \tag{1.14}$$

where $\mathbf{A}_S = [\mathbf{a}_S(\theta_1), \cdots, \mathbf{a}_S(\theta_K)]$ is the manifold matrix with

$$\mathbf{a}_S(\theta_k) = \left[1, e^{j\frac{2\pi}{\lambda} d_1 \sin(\theta_k)}, \cdots, e^{j\frac{2\pi}{\lambda} d_{M_t M_r - 1} \sin(\theta_k)}\right]^T, \tag{1.15}$$

and d_i is the distance between the i-th element of SLA and the reference element. In addition, $\mathbf{s} = [\beta_1, \cdots, \beta_K]^T$, where β_k denotes the amplitude associated with the k-th target.

Consider a virtual ULA that spans the entire array aperture and is filled with antennas spaced by interelement spacing $d = \lambda/2$. The total number of antennas in this virtual ULA is M_o and the noiseless array response is expressed as

$$\mathbf{y}_o = \mathbf{A}_o \mathbf{s}, \tag{1.16}$$

where $\mathbf{A}_o = [\mathbf{a}_o(\theta_1), \cdots, \mathbf{a}_o(\theta_K)]$ is the array manifold matrix with

$$\mathbf{a}_o(\theta_k) = \left[1, e^{j\pi \sin(\theta_k)}, \cdots, e^{j\pi(M_o - 1)\sin(\theta_k)}\right]^T. \tag{1.17}$$

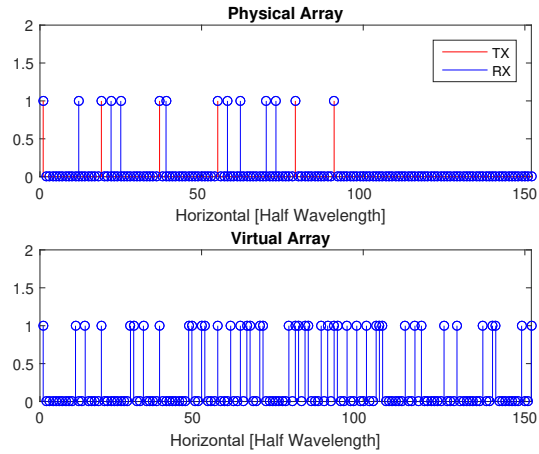

Figure 1.7 Example of an automotive radar cascaded with two transceivers. The virtual array has 48 *elements. © [2021] IEEE. Reprinted, with permission, from [5].*

Let $N_2 = \lfloor M_0/2 \rfloor$ and $N_1 = M_0 - N_2 \geq N_2$. We can formulate $\mathbf{y} \in \mathbb{C}^{M_o \times 1}$ into N_2 overlapped subarrays of length N_1. Based on those subarrays, we formulate a Hankel matrix $\mathbf{Y} \in \mathbb{C}^{N_1 \times N_2}$ with its (i,j)-th element given as $\mathbf{Y}_{ij} = \mathbf{y}_{i+j-1}$ for $i = 1, \cdots, N_1$ and $j = 1, \cdots, N_2$. The Hankel matrix $\mathbf{Y}$ has a Vandermonde factorization [63], expressed as

$$\mathbf{Y} = \mathbf{B}\Sigma\mathbf{B}^T, \tag{1.18}$$

where $\mathbf{B} = [\mathbf{b}(\theta_1), \cdots, \mathbf{b}(\theta_K)]$ is the subarray manifold matrix with

$$\mathbf{b}(\theta_k) = \left[1, e^{j\frac{2\pi}{\lambda} d \sin(\theta_k)}, \cdots, e^{j\frac{2\pi}{\lambda}(N-1) d \sin(\theta_k)}\right]^T, \tag{1.19}$$

and $\Sigma = \text{diag}(\beta_1, \cdots, \beta_K)$ is a diagonal matrix. Thus, the rank of Hankel matrix $\mathbf{Y}$ is K if $N_2 \geq K$.

We can similarly construct a Hankel matrix $\mathbf{X}$ from the SLA configuration. Unlike matrix $\mathbf{Y}$ constructed from a full ULA, however, matrix $\mathbf{X}$ has many missing entries and thus can be viewed as a subsampled version of $\mathbf{Y}$. Under certain conditions, the missing elements can be fully recovered by solving a relaxed nuclear norm optimization problem conditioned on the observed entries [64]

$$\min \ \|\mathbf{X}\|_* \quad \text{s.t.} \ \ \mathscr{P}_\Omega(\mathbf{X}) = \mathscr{P}_\Omega(\mathbf{Y}) \tag{1.20}$$

where $\|\cdot\|_*$ denotes the nuclear norm of a matrix, and $\mathscr{P}_\Omega(\mathbf{Y})$ is the sampling operator with Ω being the set of indices of observed entries that is determined by the SLA. In practice, the samples are corrupted by noise, i.e., $[\mathbf{X}]_{ij} = [\mathbf{Y}]_{ij} + [\mathbf{E}]_{ij}, (i,j) \in$

Ω, where $[\mathbf{E}]_{ij}$ denotes the noise. In this case, the matrix completion problem is formulated as

$$\min \|\mathbf{X}\|_* \quad \text{s.t.} \quad \|\mathscr{P}_\Omega(\mathbf{X}-\mathbf{Y})\|_{\mathrm{F}} \leq \delta \tag{1.21}$$

where $\|\cdot\|_{\mathrm{F}}$ denotes the Frobenius norm of a matrix and δ is a constant determined by the noise power.

Once the matrix $\mathbf{Y}$ is recovered, the full array response is obtained by averaging its anti-diagonal entries. DOAs can be estimated via standard array processing methods based on the array response corresponding to the completed matrix $\mathbf{Y}$.

To achieve high azimuth angular resolution, multiple automotive radar transceivers are cascaded together to synthesize a large sparse array in azimuth. Here, we consider the same physical array shown in Fig. 1.7, where $M_t = 6$ transmit and $M_r = 8$ receive antennas are placed in an interleaved way along the horizontal direction at

$$l_{\mathrm{TX}} = [1, 19, 37, 55, 79, 91]\,\lambda/2,$$
$$l_{\mathrm{RX}} = [12, 22, 25, 39, 58, 62, 70, 73]\,\lambda/2.$$

A virtual array with total 48 elements is synthesized. The transmit and receive antennas as well as the virtual array are plotted in Fig. 1.7.

Two targets are at the same range $R = 100$ m with velocity of $v = -10$ m/s. Their respective azimuth angles are $\theta_1 = 0^\circ$ and $\theta_2 = 20^\circ$. The two targets are first separated in range-Doppler. The complex peak values in the range-Doppler spectrum corresponding to every virtual sparse array consists of an array snapshot for azimuth angle finding.

The virtual SLA shown in Fig. 1.7 acts as a deterministic sampler of a rank-2 Hankel matrix $\mathbf{Y} \in \mathbb{C}^{N\times N}$ with $N = 76$, which is constructed based on the array response of a ULA with 152 elements. The array response of the SLA is normalized by its first element. Based on the observed SLA response, the Hankel matrix $\mathbf{Y}$ is completed via the SVT algorithm [65]. Let $\hat{\mathbf{Y}}$ denote the completed Hankel matrix. The full ULA response can be reconstructed by taking the average of the anti-diagonal elements of matrix $\hat{\mathbf{Y}}$. The completed full array has an aperture size of 76λ. Intuitively, in this simulation setting, matrix completion contributes around $10\log 10\left(152/48\right) \approx 5$ dB SNR improvement for array processing.

In Fig. 1.8, we plot the angle spectrum for the two targets. The two azimuth angle spectra are obtained by applying FFT to the original SLA with the holes filled with zeros and to the full array completed via matrix completion, respectively. It is found that the FFT of the SLA generates two peaks corresponding to the correct azimuth directions at a cost of high sidelobes, and thus it is difficult to detect the two targets in azimuth directions under the original SLA. On the contrary, the completed full array shows two clear peaks corresponding to correct azimuth locations in the angle spectrum, and the sidelobes are greatly suppressed in the completed full array.

1.3.2.2 Two Dimensional Sparse Array Interpolation via Matrix Completion

To enable driver-over and driver-under functions, automotive radar must measure target's elevation angles accurately. As a result, automotive radar needs to provide

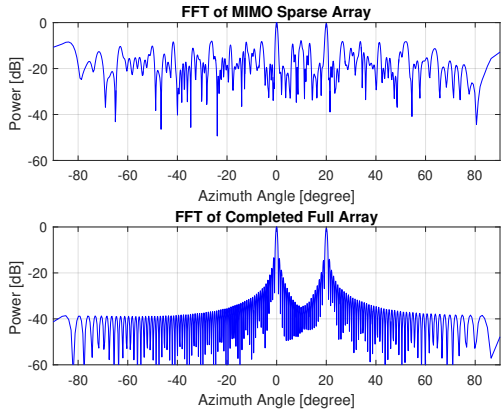

Figure 1.8 The spectrum of two targets with azimuth angles of $\theta_1 = 0^\circ$ and $\theta_2 = 20^\circ$ degree under MIMO sparse array and fully completed array. © [2021] IEEE. Reprinted, with permission, from [5].

point clouds with high angular resolution in both azimuth and elevation directions. Fig. 1.9 shows a MIMO radar with 12 transmit antennas and 16 receive antennas that are obtained by cascading 4 automotive radar transceivers, and the transmit and receive antennas are randomly deployed in an area of $[0,100]\,(\lambda/2) \times [0,120]\,(\lambda/2)$ to synthesize a MIMO 2D virtual sparse array of 196 elements. The 2D physical array corresponds to a form factor of about 20×24 cm when the carrier frequency is $f_c = 77$ GHz. It should be noted that a tradeoff between the angular resolution and the radar form factor should be considered in practice so that the radar can be incorporated behind vehicle bumper. The dimension of the rendered 2D virtual sparse array is $D_y \times D_x = 183(\lambda/2) \times 194(\lambda/2)$, which can be viewed as a spatial sub-Nyquist sampling of a uniform rectangular arrays (URA) of the same dimension with half-wavelength spacing in both horizontal and vertical directions. The azimuth and elevation angular resolutions are respectively expressed as [43]

$$\Delta\theta = 2\arcsin\left(\frac{1.4\lambda}{\pi D_x}\right) \approx 0.53^\circ, \tag{1.22}$$

$$\Delta\phi = 2\arcsin\left(\frac{1.4\lambda}{\pi D_y}\right) \approx 0.56^\circ. \tag{1.23}$$

The angular resolution of imaging radar in this example is comparable to the Velodyne LiDAR HDL-32E whose horizontal resolution is between 0.1° and 0.4° depending on the rotation rate, and the vertical resolution is 1.33° [66].

Consider a general case of an $M_1 \times M_2$ URA with half-wavelength spacing, shown in Fig. 1.10, where the URA is on the x-y plane. Assume the k-th point target with azimuth angle θ_k and elevation angle ϕ_k. Let χ_k denote the angle between the k-th target and the x axis, and φ_k denote the angle between the k-th target and the y axis. Then, it holds that $\cos(\chi_k) = \sin(\phi_k)\cos(\theta_k)$, $\cos(\varphi_k) = \sin(\phi_k)\sin(\theta_k)$.

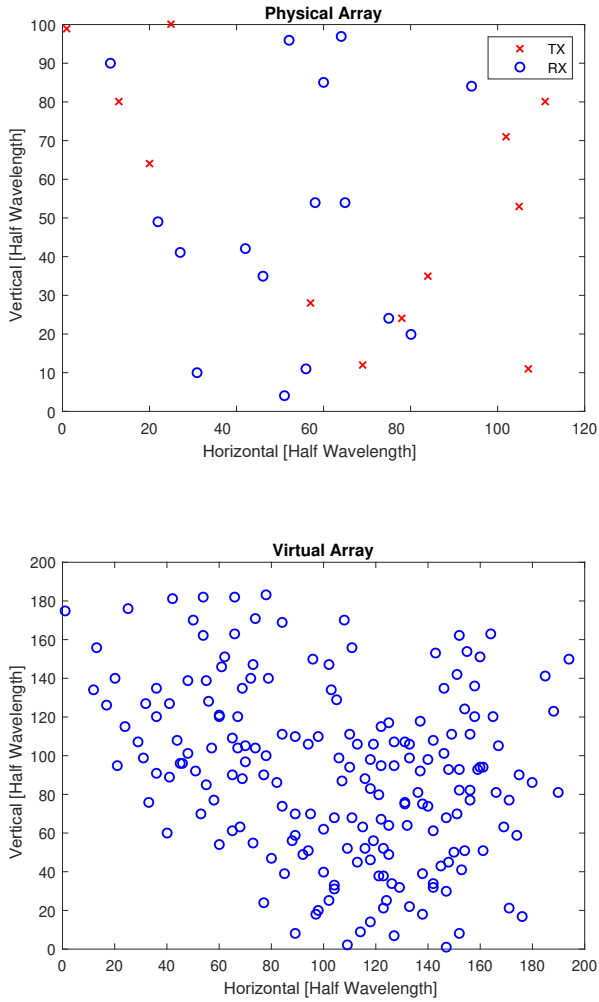

Figure 1.9 *A MIMO radar with* 12 *transmit antennas and* 16 *receive antennas by cascading* 4 *automotive radar transceivers. The transmit and receive antennas are randomly deployed in an area of* $[0,100]\,(\lambda/2) \times [0,120]\,(\lambda/2)$ *to synthesize a MIMO 2D virtual array of* 196 *elements. © [2021] IEEE. Reprinted, with permission, from [5].*

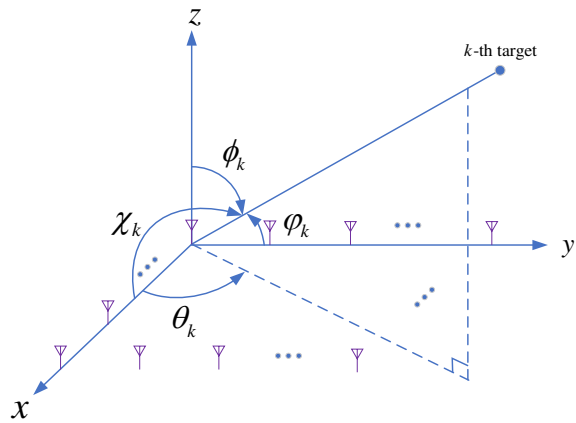

Figure 1.10 *Geometry of URA. © [2021] IEEE. Reprinted, with permission, from [5].*

Therefore,

$$\theta_k = \arctan\left(\frac{\cos(\varphi_k)}{\cos(\chi_k)}\right), \tag{1.24}$$

$$\phi_k = \arcsin\left(\sqrt{\cos^2(\chi_k)+\cos^2(\varphi_k)}\right). \tag{1.25}$$

Once the angles χ_k and φ_k are known, the azimuth angle θ_k and elevation angle ϕ_k can be uniquely determined. To simplify the signal modeling, we use angles χ_k and φ_k for signal modeling in URA.

The (m_1, m_2)-th element of the URA array on the x-y plane response with respect to K targets with angle to the x-axis χ_k and angle to the y-axis φ_k, $k = 1, ..., K$, can be written as

$$x_{m_1,m_2} = \sum_{k=1}^{K} \beta_k e^{j\pi((m_1-1)\sin(\chi_k)+(m_2-1)\sin(\varphi_k))} \tag{1.26}$$

for $1 \le m_1 \le M_1$ and $1 \le m_2 \le M_2$. Let $\mathbf{M} = \left[x_{m_1,m_2}\right]_{0\le m_1\le M_1, 0\le m_2\le M_2}$ be the data matrix with entries as the URA array response defined in (1.26). We can construct an $N_1 \times (M_1 - N_1 + 1)$ block Hankel matrix as

$$\mathbf{Y}_E = \begin{bmatrix} \mathbf{Y}_0 & \mathbf{Y}_1 & \cdots & \mathbf{Y}_{M_1-N_1} \\ \mathbf{Y}_1 & \mathbf{Y}_2 & \cdots & \mathbf{Y}_{M_1-N_1+1} \\ \vdots & \vdots & \ddots & \vdots \\ \mathbf{Y}_{N_1-1} & \mathbf{Y}_{N_1} & \cdots & \mathbf{Y}_{M_1-1} \end{bmatrix}, \tag{1.27}$$

where

$$\mathbf{Y}_m = \begin{bmatrix} x_{m,0} & x_{m,1} & \cdots & x_{m,M_2-L} \\ x_{m,1} & x_{m,2} & \cdots & x_{m,M_2-L+1} \\ \vdots & \vdots & \ddots & \vdots \\ x_{m,L-1} & x_{m,L} & \cdots & x_{m,M_2-1} \end{bmatrix}, \tag{1.28}$$

is an $L \times (M_2 - L + 1)$ Hankel matrix. It can be verified that the rank of matrix $\mathbf{Y}_E$ is K if $N_1 \geq K$ and $L \geq K$ [67].

By choosing the locations of the transmit and receive antennas, we aim to synthesize a sparse 2D array, which can be viewed as spatial subsampling of the URA. The array response of the URA can be obtained via completing the block Hankel matrix $\mathbf{Y}_E$ based on the array response of sparse arrays. The block Hankel matrix completion problem is formulated as

$$\min \|\mathbf{X}_E\|_* \quad \text{s.t.} \quad \mathscr{P}_\Omega(\mathbf{X}) = \mathscr{P}_\Omega(\mathbf{M}) \tag{1.29}$$

where Ω denotes the observation set consisting of the location of 2D sparse virtual array elements, and $\mathbf{X}_E$ is the block Hankel matrix constructed from matrix $\mathbf{X}$ following equations (1.27) and (1.28). In the noisy observation scenario, $\mathbf{M}$ is replaced by $\mathbf{M}^o = \left[x^o_{m_1,m_2}\right]_{0\leq m_1\leq M_1, 0\leq m_2\leq M_2}$ with $x^o_{m_1,m_2} = x_{m_1,m_2} + n_{m_1,m_2}$, where $x^o_{m_1,m_2}$ denotes the observed signal and $\mathbf{E} = \left[n_{m_1,m_2}\right]_{0\leq m_1\leq M_1, 0\leq m_2\leq M_2}$ is the noise term. We assume the noise is bounded, i.e., $\|\mathscr{P}_\Omega(\mathbf{E})\|_{\mathrm{F}} \leq \delta$. The noisy block Hankel matrix completion problem is formulated as

$$\min \|\mathbf{X}_E\|_* \quad \text{s.t.} \quad \left\|\mathscr{P}_\Omega\left(\mathbf{X} - \mathbf{M}^o\right)\right\|_{\mathrm{F}} \leq \delta. \tag{1.30}$$

The above optimization problem can be solved in CVX toolbox [68]. In the simulation, we adopt the singular value thresholding (SVT) algorithm [65] to solve the matrix completion problems, whose computation cost of updating the low-rank matrix in each iteration is of order m with m being the cardinality of the observation set Ω, i.e., $m = |\Omega|$.

We consider the same 2D physical array shown in Fig. 1.9 for joint high-resolution azimuth and elevation angle estimation, by cascading 4 automotive radar transceivers. These 12 transmit antennas and 16 receive antennas are randomly deployed in an area of $[0, 100(\lambda/2)] \times [0, 120(\lambda/2)]$ to synthesize a 2D MIMO virtual array of 196 elements. The cascaded automotive radar form factor is around 20×24 cm. In Fig. 1.9, the dimension of the 2D sparse array is $D_y \times D_x = 183(\lambda/2) \times 194(\lambda/2)$. A total number of $35,502$ elements are required to construct a URA of the same dimension with half-wavelength interelement spacing. In other words, the virtual sparse array only occupies 0.54% the total elements of the URA.

Two targets with the same range and Doppler bin are considered. Their angles to the x and y directions are $(\chi_1, \varphi_1) = \left(-20^\circ, 5^\circ\right), (\chi_2, \varphi_2) = \left(20^\circ, 10^\circ\right)$, respectively. The sparse array snapshot is consisted of the complex peak values in the range-Doppler spectrum corresponding to each sparse array element. The input SNR of

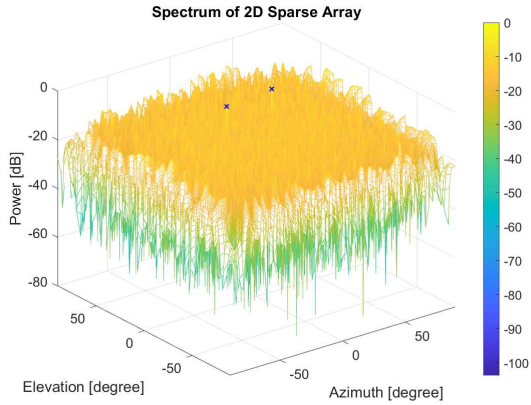

Figure 1.11 *The spectrum of two targets with azimuth and elevation angles of* $(\chi_1, \varphi_1) = (-20^\circ, 5^\circ), (\chi_2, \varphi_2) = (20^\circ, 10^\circ)$ *under the sparse array. The targets' angles are marked with crosses. There are high sidelobes in the spectrum due to the existing of large number of holes in the sparse array. © [2021] IEEE. Reprinted, with permission, from [5].*

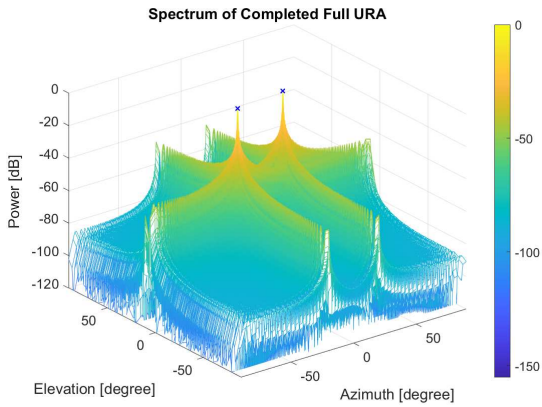

Figure 1.12 *The spectrum of two targets with azimuth and elevation angles of* $(\chi_1, \varphi_1) = (-20^\circ, 5^\circ), (\chi_2, \varphi_2) = (20^\circ, 10^\circ)$ *under the completed full URA. The targets' angles are marked with crosses. © [2021] IEEE. Reprinted, with permission, from [5].*

the array response is set to 20 dB, which is reasonable in automotive radar because the fast-time and slow-time coherent processing provides a high processing gain. We then construct a block Hankel matrix $\mathbf{Y}_E$ of dimension $9,009 \times 8,928$ using one array snapshot of this 2D sparse array with 196 elements. Only 0.78% of the Hankel matrix entires are non-zero. Based on one snapshot of 2D sparse array, the block Hankel matrix is completed via the SVT algorithm and the full URA is then obtained. In this simulation setting, matrix completion contributes around $10\log 10\left(35,502/196\right) \approx$ 22.5 dB SNR gain for array processing.

Figs. 1.11 and 1.12 plot the azimuth-elevation spectra of the two targets under the 2D sparse array and the completed full URA, respectively. It is found that both sparse array and URA generate two peaks corresponding to the correct azimuth and elevation angles of the targets. However, in the azimuth-elevation spectrum of 2D sparse array, there are high sidelobes over the entire azimuth and elevation FOVs. On the contrary, the high sidelobes are mitigated in the completed URA.

1.3.2.3 Sparse Linear Array Optimization

Alternatively, instead of filling the holes, angle finding of the sparse array can be done using spatial compressive sensing (CS) ideas [69]. In that context, the key problems are how to select the locations of array elements such that the peak sidelobe level (PSL) of the virtual SLA beampattern is low, and how to carry out angle finding. There is no analytical solution to determining the antenna locations that achieve a minimum PSL for a given number of antennas [70]. Optimal sparse array design requires global optimization techniques, such as particle swarm optimization [71, 45, 72].

In the SLA scenario, it can be easily verified that the coherence of the basis matrix (see (1.9)), is the PSL of the SLA array beampattern [44]. Therefore, the coherence, or equivalently, the PSL of a sparse array plays a key role in obtaining uniform recovery guarantees for compressive sensing [54]. If the PSL of SLAs is low, angle finding using SLAs can be done via compressive sensing or IAA.

In Fig. 1.13, we give an example of a virtual SLA with aperture of 19λ, synthesized with MIMO radar technology using 4 transmit 4 receive antennas. The first and fourth of transmit/receive antennas are deployed at the edge of the physical aperture, while the remaining antennas are chosen such that the PSL is -9.1dB. Angle estimation via IAA when using the sparse linear array of Fig. 1.13 is illustrated in Fig. 1.14. The ground truth involves two targets with azimuth 5° and 10°. The SNR of the received beamvector is set to 30dB. For comparison, the FFT spectrum is also plotted. One can observe the sharper peaks around the target azimuth angles and the more attenuated sidelobe in the IAA spectrum, as compared to the FFT spectrum.

1.4 High Resolution Imaging Radar for Autonomous Driving

Nowadays, many of the automotive radar transceivers designed for ADAS functionality, such as MR3003 of NXP Semiconductor, and AWR2243 of Texas Instruments, can support up to 3 transmit and 4 receive antennas. Therefore, using a single automotive radar transceiver with MIMO radar technology, only 12 virtual array ele-

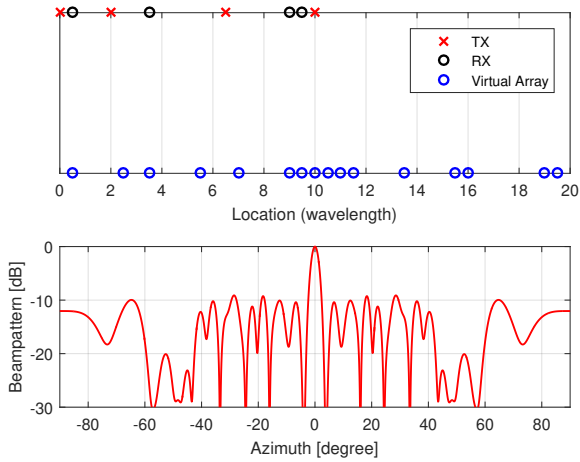

Figure 1.13 *Simulated example of a SLA synthesized with MIMO radar technology using four transmit and four receive antennas. The physical limitation of array aperture is* 10λ*. We fix the locations of first and fourth transmit/receive antennas at* $0\lambda, 0.5\lambda$ *and* $10\lambda, 9.5\lambda$*, respectively such that a maximum virtual array aperture of* 19λ *is achieved. The remaining transmit/receive antennas are chosen such that the PSL of the synthetic virtual array beampattern is* -9.1dB. © *[2020] IEEE. Reprinted, with permission, from [6].*

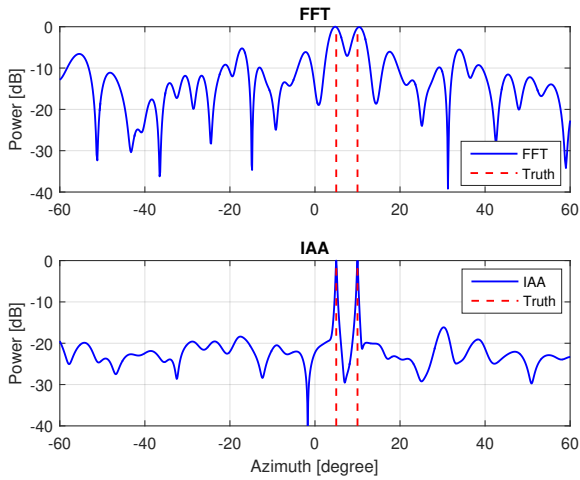

Figure 1.14 *Angle finding via the IAA method and the FFT spectrum using the SLA of Fig. 1.13, synthesized by MIMO radar technology. There are two targets with azimuth of* 5° *and* 10°*. The SNR is set to* 30dB. © *[2020] IEEE. Reprinted, with permission, from [6].*

ments can be synthesized. In this section, we introduce the high resolution imaging radar with hundreds of virtual antenna array elements synthesized via MIMO radar technology.

1.4.1 Cascade of multiple radar transceivers

To meet the requirement for Level 4 and Level 5 autonomous driving, multiple automotive radar transceivers would need to be cascaded together, with all transceivers synchronized as a single unit. The received data from all receive antennas would be processed coherently. Cascading provides a cost effective and scalable solution to achieve high angular resolution. In [73], General Motors and Texas Instruments successfully demonstrated that up to 4 Texas Instruments AWR1243 radar chips can be cascaded together to provide 12 transmit and 16 receive antennas, enabling a synthesis of 192 virtual array elements. In [74], a prototype of cascading 5 Infineon radar chips has been built to synthesize a virtual array of 128×4 elements. Such high number of virtual array elements provides a lot of opportunities in array design. Several azimuth and elevation arrays configurations can be found in [60]. Several commercial imaging radar products are available with different array configurations, such as forward-looking full-range radar of ZF and ARS540 of Continental [75, 76]. Usually, a trade-off of balancing angular resolution in azimuth and elevation needs to be considered.

1.4.2 Examples of cascaded imaging radars

Figure 1.15 shows an imaging radar design reference board which has 12 transmit and 16 receive antennas, formed by cascading 4 Texas Instruments AWR2243 radar transceivers [77]. The azimuth FOV is $\left[-70^{\circ}, 70^{\circ}\right]$. One transceiver is selected as master and all the others as slaves for clock distribution. In this way, synchronization can be achieved among 4 transceivers, allowing coherent FMCW transmission from the 12 transmit antennas and joint data processing from the 16 receive antennas. The array configuration of cascaded imaging radar is shown in Fig. 1.15. There are 3 transmit antennas placed along the vertical direction for elevation angle finding, and 9 transmit antennas placed along the horizontal direction for azimuth angle finding. The virtual array in the horizontal direction is a dense ULA with half wavelength spacing, and consists of 86 virtual array elements (the overlapped virtual array elements are not shown). The array aperture in the azimuth direction is $D_x = 42.5\lambda$. In antenna theory, the 3dB beamwidth defines the angular resolution. According to [43], the 3dB beamwidth of the azimuth angle is

$$\Delta\theta_{\mathrm{AZ}} = 2\arcsin\left(\frac{1.4\lambda}{\pi D_x}\right) \approx 1.2^{\circ}. \tag{1.31}$$

In the vertical direction, the antennas in three elevation positions form multiple minimum redundancy arrays (MRAs) [78] along the horizontal direction. The angle finding in MRA requires multiple snapshots. These MRAs along the horizontal direction can be used as snapshots for elevation angle finding. The elevation array

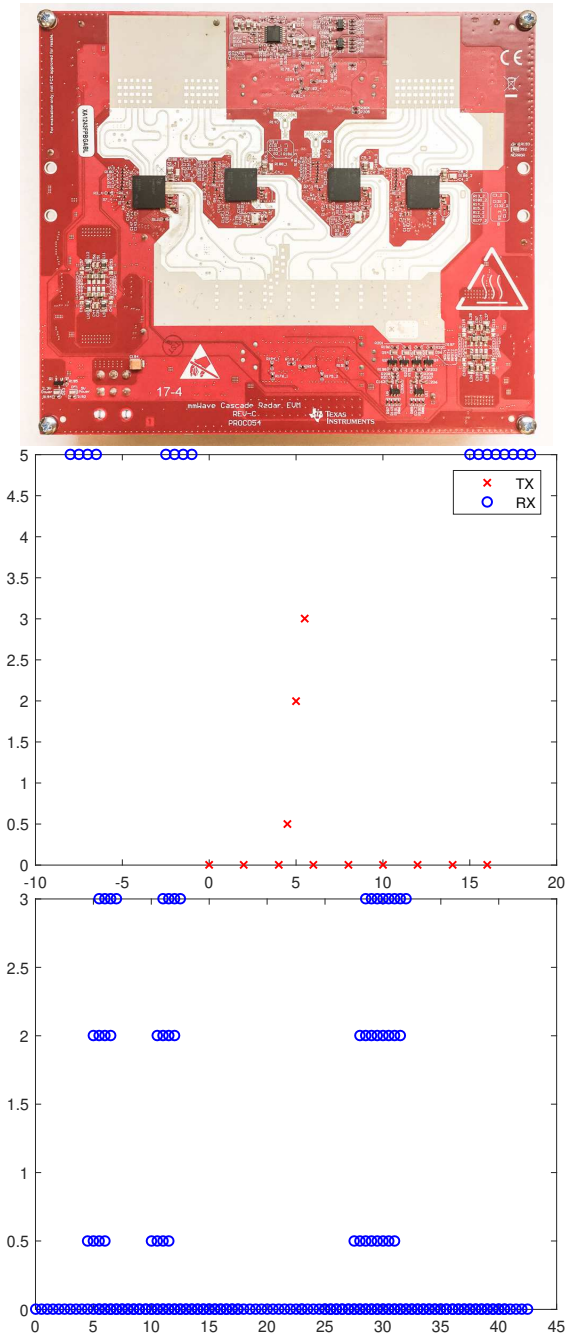

Figure 1.15 Texas Instruments AWR2243 imaging radar board (top figure) [77]. 4 *TI AWR2243 radar transceivers are cascaded together, providing* 12 *transmit and* 16 *receive antennas (middle figure), enabling the synthesis of* 192 *virtual array elements (bottom figure). © [2020] IEEE. Reprinted, with permission, from [6].*

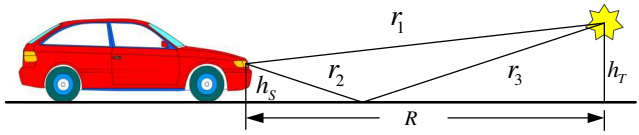

Figure 1.16 Direct path and vertical multipath. © [2020] IEEE. Reprinted, with permission, from [6].

aperture is $D_y = 3\lambda$ and the 3dB beamwidth of elevation is

$$\Delta\theta_{\mathrm{EL}} = 2\arcsin\left(\frac{1.4\lambda}{\pi D_y}\right) \approx 17^{\circ}. \tag{1.32}$$

1.4.3 Design challenges of imaging radar

Achieving waveform orthogonality in imaging radars using FMCW with a large of number transmit antennas is quite challenging. One strategy could be to divide the transmit antennas into several subgroups. In each subgroup, the transmit antennas would transmit simultaneously with slow-time phase coding (DDM), while antennas of different subgroups would be scheduled to transmit in different time slots (TDM).

Clock distribution among multiple cascaded transceivers is also challenging. For FMCW mixer operation, an LO is shared among master and slaves, and the LO routing from master to all slaves in the circuit should be matched. Also, the additional ADC sampling and data transmission among different transceivers needs to be synchronized. It is desirable to develop automotive radar transceiver that can incorporate a large number of transmit and receive antennas. For example, Uhnder has developed a radar system-on-chip (SoC), which has 12 transmit and 16 receive antennas, enabling synthesis of 192 virtual array elements [79] (discussed in more detail in later chapters) . Thus, the 4 current automotive radar transceivers in the cascaded imaging radar shown in Fig. 1.15 can be replaced with a single SoC radar chip. The radar on chip (RoC) developed by Vayyar has 48 transceivers at 76-81GHz, which can provide synthesis over 2000 virtual array elements [80].

1.5 Challenges in Automotive MIMO radar

In this section, we discuss the design challenges in automotive MIMO radar, including angle finding in the presence of multipath reflections, waveform orthogonality and efficient high resolution angle estimation algorithm development.

1.5.1 Angle finding in the presence of multipath reflections

Automotive radar runs in multipath scenarios [81]. In general, radio propagation in the presence of multipath occurs along four possible routes, i.e., direct/direct, direct/indirect, indirect/direct and indirect/indirect routes.

Figure 1.16 shows a vertical multipath scenario, where the height of radar and target are h_S and h_T, respectively. The length of the direct/direct path is $d_1 = 2r_1$, the length of the direct/indirect or indirect/direct path is $d_2 = d_3 = r_1 + r_2 + r_3$, and the length of the indirect/indirect path is $d_4 = 2(r_2 + r_3)$. The received signal, having gone through the four paths can be written as

$$y_r = \sum_{i=1}^{4} \beta_i e^{j\frac{2\pi}{\lambda} d_i}, \tag{1.33}$$

where the amplitude term β_i is function of the antenna gain, the path loss, the road reflection coefficient and the target RCS. The signal from the indirect paths and that from the direct path would most probably arrive out of phase and thus add up destructively. As a result, the power of the received signal would fluctuate with distance [81] and thus angle finding at SNR nulls would be unstable.

MIMO radar with colocated transmit and receive antennas, also referred to as monostatic MIMO radar, is based on the assumption that DOD and DOA are equal. However, in the presence of multipath, that assumption does not hold and the system becomes bistatic [82, 83], i.e., the transmit and receive antenna view the target from different aspect angles. Fig. 1.17 shows a vehicle moving parallel to the guardrail, with an SRR sensor mounted at its front left corner. The length of the direct path of the radar signal is $d_{r_1} = r_1$, corresponding to $\theta_t = \theta_r = \theta_1$. There are also multipath reflections due to the guardrail. The range of the first multipath reflection is $d_{r_2} = (r_1 + r_2 + r_3)/2$, corresponding to $\theta_t = \theta_1, \theta_r = \theta_2$ or $\theta_t = \theta_2, \theta_r = \theta_1$. The range of the second multipath reflection is $d_{r_3} = r_2 + r_3$, corresponding to $\theta_t = \theta_r = \theta_2$. Compared to the direct path, multipath reflections result in longer range and smaller Doppler. For the first type of multipath, the range and Doppler bin is the same as in mirror image target detection. However, as $\theta_t \neq \theta_r$, it turns out that the phase of each virtual array element is corrupted. In other words, the monostatic MIMO radar assumption does not hold, which results in a "ghost" target whose direction is different from the mirror target.

To solve this issue, some ideas have been proposed in [82, 83, 84]. For example, joint estimation of DOD and DOA is proposed in [82], however, by ignoring the structure of the transmit array, that method cannot not enjoy the benefit of the synthesized virtual array. Polarimetric features are exploited in [83] to separate objects in a multipath scenario. However, the approach in [83] can only separate certain real target cases from their mirror targets, for example, when the real target is known and the polarization state change of the multipaths can be recognized. The method of [83] does not work when the ghost target direction is different than that of the mirror target. Doppler information can be exploited to detect moving vehicles in urban areas under multipath [84]. However, Doppler information is not always available when both objects and host vehicles are stationary. In general, there is a need for more research addressing ghost target issue in MIMO radar due to multipath.

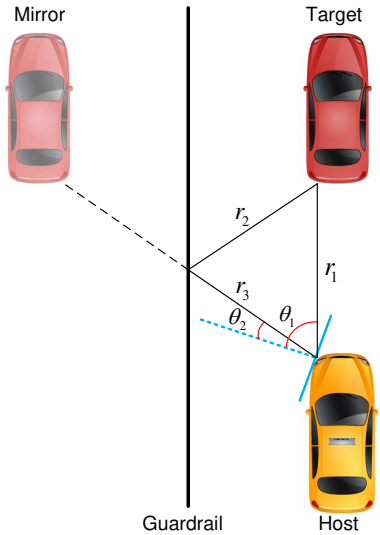

Figure 1.17 A typical multipath reflection scenario along a guardrail for a short range radar sensor mounted at the front left corner. © [2020] IEEE. Reprinted, with permission, from [6].

1.5.2 Waveform orthogonality in automotive MIMO radar

Different strategies, such as TDM, DDM and FDM can be adopted in automotive FMCW radars to achieve waveform orthogonality. However, several challenges associated with each strategy need to be addressed. For example, in the TDM scheme, the scheduling delay between transmit antennas may introduce phase error for a moving target, which needs to be compensated for, otherwise, the synthesized array beampattern will be distorted. Further, the maximum unambiguous detectable velocity under TDM is reduced by a factor of M_t. In the DDM scheme, the Doppler sidelobes are high due to the residual of the phase coding. As a result, targets with small RCSs, e.g., pedestrians, that are close to the target with strong reflections, e.g., trucks, might be masked. The search time for phase codes using stochastic algorithms increases exponentially as the code length increases. Computationally efficient algorithms are needed to address this problem. In the FDM scheme, though a randomization of frequency shift among transmit antennas could reduce the range-angle coupling, a large number of transmit antennas would be needed for the improvement to be notable [16].

Recently, PMCW has been proposed for achieving orthogonality [85, 86, 87, 88]. Each antenna transmits a sequence of phase coded pulses. Let

$$\mathbf{x}_m = \left[x_m(1), \cdots, x_m\left(N_p\right)\right]^T \tag{1.34}$$

be the complex unimodular code sequence of the m-th transmit antenna, where $x_m(n) = e^{j\phi_m(n)}$ is the n-th code of $\mathbf{x}_m$ and N_p is the code length. Here, the phase $\phi_m(n)$ can be chosen arbitrarily in $[-\pi, \pi]$. The duration of a single code sequence

is $T_p = N_p T_c$ with T_c the duration of a sub-pulse. In practice, binary code sequences have been widely used due to their simplicity. The bandwidth of PMCW is $B = 1/T_c$. The time-bandwidth product of a code sequence is $BT_p = N_p$. Since the pulses are transmitted continuously, the code sequences should have good periodic auto-correlation and cross-correlation properties [85]. The periodic cross-correlation of two code sequences $\mathbf{x}_m$ and $\mathbf{x}_l$ at lag k is defined as

$$r_{ml}^{\mathscr{P}}(k) = \sum_{n=1}^{N} x_m(n) x_l^*\left((n+k) \bmod \left(N_p\right)\right). \tag{1.35}$$

When $m = l$, $r_{ml}^{\mathscr{P}}(k)$ becomes the periodic auto-correlation function of $\mathbf{x}_m$. Good correlation properties require the values of the periodic auto-correlation at non-zero lags, and the values of the cross-correlation at any lag to be low. The Welch lower bound on the cross-correlation between any pair of binary sequences with period of N_p in a set of M_t sequences equals [89]

$$r_{ml}^{\mathscr{P}}(k) \geq N_p \sqrt{\frac{M_t - 1}{M_t N_p - 1}} \approx \sqrt{N_p}. \tag{1.36}$$

Good periodic cross-correlation properties help achieve waveform orthogonality, while good periodic auto-correlation properties make it easier to use matched filters to extract signals reflected from the range bin of interest and suppress signals reflected from other range bins.

As compared to FMCW, PMCW radar has several advantages. PMCW radar is better suited for achieving waveform orthogonality in imaging radars with a large of number of transmit antennas. PMCW radar can take advantage of existing sequences with good auto-correlation and cross-correlation properties, previously developed for code-division multiple accessing (CDMA) communications, such as Gold, Kasami and m-sequences [90, 91, 92]. Further, in PMCW radar, each automotive radar sensor can have a unique digital sequence, which may help reduce the automotive radar mutual interference. As a bonus, PMCW radar also provides certain communication capability [93], thus can be explored as a dual functional radar communication system [94].

However, PMCW radar has many implementation challenges. First, the sampling rate of ADC should satisfy the Nyquist rule, i.e., $f_s \geq 2B = 2/T_c$. The high bandwidth required for high range resolution necessitates high speed ADC and high speed processing hardware. In practice, it is required to keep the resolution of ADC as low as possible [95]. Second, according to the Welch bound of (1.36), the cross-correlation lower bound of any pair of binary sequences is of the order of $\mathscr{O}\left(\sqrt{N_p}\right)$, which might not provide sufficient separation of transmit waveforms of different antennas. In practice, the auto-correlation and cross-correlation of code sequences are desired to have low sidelobes within a low correlation zone (LCZ). Furthermore, because there is no mapping relationship between range and beat signal in PMCW, it would be difficult to use high-pass analog filters to reject or attenuate ultra-close-range return signals, including direct path signals from transmit antennas, reflections

from Radome, and vehicle bumpers. This escalates the dynamic range challenge, especially when the resolution of ADC must be kept as low as possible [95].

1.5.3 Efficient, high resolution angle finding algorithms are needed

A typical duration of a look in automotive radar is around 50 ms, corresponding to detection update rate of 20 Hz [96]. In such short duration, the current generation of automotive radar for ADAS can report a maximum of $64-200$ detections. With high resolution imaging radar, the number of cells that can be selected for angle finding from the 2D range and Doppler spectrum is around $10,000$ in a single look for a typical road scenario [62]. To achieve point clouds for autonomous driving, angle finding needs to be performed thousands of times in a single look, which is a great challenge for imaging radar with hundreds of virtual array elements. Computationally efficient, high resolution angle finding algorithms are highly desirable for real-time implementation in automotive radar.

To reduce computation complexity, beamspace ESPRIT [28] and unitary ESPRIT [29] algorithms have been proposed. The idea of beamspace ESPRIT is to decompose the original ULA vector into several low-dimensional beamspaces via a transform such as the FFT. Then, if the beamspace transform matrix has the same shift invariance structure, angle finding can be carried out via ESPRIT on each beamspace in parallel, with reduced computational time [28]. The unitary ESPRIT algorithm takes advantage of the unit magnitude property of the phase factors representing the phase delays between the two subarrays and is formulated in terms of real-valued computations. As a result, it achieves great reduction of computational complexity [29].

The computation cost of each IAA iteration is $2NM^2+NM+M^3$, where M is the number of array snapshots and N is the number of discretized grids. Fast and superfast IAA algorithms have been proposed in [97, 98, 99], respectively. The fast IAA algorithm exploits the FFT operation as well as Gohberg-Semencul (GS) representation of matrix $\mathbf{R}^{-1}$. As a result, the computation cost of each fast IAA iteration is $M^2+12\zeta(2M)+3\zeta(N)$, where $\zeta(N)$ stands for the computation cost of performing FFT of size N, i.e., $O(N\log N)$ [98]. The superfast IAA uses a conjugate gradient (CG) algorithm to approximate the matrix $\mathbf{R}^{-1}$, which further reduces the computation cost.

The strengths and limitations of each DOA estimation algorithm discussed in Section 1.3 when applied to the automotive radar scenario are summarized in Table 1.1. For subspace based high resolution DOA estimation methods, such as MUSIC and ESPRIT, the automotive radar array needs to be ULA, and multiple snapshots are required to estimate the array covariance matrix accurately. However, automotive radar operating in a highly dynamic environment typically rely on a single snapshot. While multiple snapshots can generated via spatial smoothing or by dividing a chirp into sub-chirps, the associated cost is respectively reduced array aperture, or reduced SNR. SLAs have been widely used in automotive radar to further reduce the hardware cost. However, it is not straightforward to apply MUSIC or ESPRIT to SLA based automotive radar. On the other hand, DBF and sparsity based high resolution

Algorithms	Resolution	Snapshot	Arrays	Grid Free	Rank Estimation	Robustness	Complexity
DBF	low	single	ULA/SLA	no	no	strong	low
MUSIC	high	multiple	ULA	no	yes	medium	high
ESPRIT	high	multiple	ULA	yes	yes	medium	medium
OMP	high	single	ULA/SLA	no	no	medium	high
IAA	high	single	ULA/SLA	no	no	strong	high

Table 1.1 Summary of different DOA estimation algorithms in automotive radar scenario.

methods, such as OMP and IAA, apply to SLA- as well as ULA-based automotive radar, and work with a single snapshot. In the DBF method, the number of targets can be estimated by counting the number of peaks in the DOA spectrum. DBF is not sensitive to coherent or correlated signals, which in subspace based methods [100] need special preprocessing via spatial smoothing. It has been shown that DBF is robust to array element position errors and has low computational cost [100]. However, DBF is not a high resolution method. Also, as OMP and IAA are iterative schemes, they involve high computation cost, which limits their applicability in low-cost embedded DSPs typically used in current generation automotive radar. Further, the methods of DBF, MUSIC, OMP and IAA assume targets are on the grid, and suffer from errors when the targets arise between grid points. In summary, more research is needed on developing computationally efficient, high resolution DOA estimation algorithms that are robust to noise, and are applicable to automotive radar using SLAs with low PSL under a single snapshot.

References

[1] C. R. Qi and et al., "PointNet: Deep learning on point sets for 3D classification and segmentation," in *Proc. the IEEE Conference on Computer Vision and Pattern Recognition (CVPR)*, (Honolulu, HI), July 2017.

[2] C. R. Qi, L. Yi, H. Su, and L. J. Guibas, "PointNet++: Deep hierarchical feature learning on point sets in a metric space," in *Proc. 31st Conference on Neural Information Processing Systems (NIPS)*, (Long Beach, CA), Dec. 2017.

[3] S. Brisken, F. Ruf, and F. Hohne, "Recent evolution of automotive imaging radar and its information content," *IET Radar, Sonar & Navigation*, vol. 12, no. 10, pp. 1078–1081, 2018.

[4] A. Danzer, T. Griebel, M. Bach, and K. Dietmayer, "2D car detection in radar data with PointNets," *arXiv:1904.08414*, July 2019.

[5] S. Sun and Y. D. Zhang, "4D automotive radar sensing for autonomous vehicles: A sparsity-oriented approach," *IEEE J. Sel. Topics Signal Process.*, vol. 15, no. 4, pp. 879–891, 2021.

[6] S. Sun, A. P. Petropulu, and H. V. Poor, "MIMO radar for advanced driver-assistance systems and autonomous driving: Advantages and challenges," *IEEE Signal Process. Mag.*, vol. 37, no. 4, pp. 98–117, 2020.

[7] J. Bergin and J. R. Guerci, *MIMO Radar: Theory and Application*. Boston, MA, Artech House, 2018.

[8] A. Duly, D. Love, and J. Krogmeier, "Time-division beamforming for MIMO radar waveform design," *IEEE Trans. Aerosp. Electron. Syst.*, vol. 49, no. 2, pp. 1210–1223, 2013.

[9] K. Rambach and B. Yang, "Colocated MIMO radar: Cramer-Rao bound and optimal time division multiplexing for DOA estimation of moving targets," in *Proc. IEEE 38th Int. Conf. on Acoustics, Speech, and Signal Processing (ICASSP)*, (Vancouver, Canada), May 2013.

[10] D. Zoeke and A. Ziroff, "Phase migration effects in moving target localization using switched MIMO arrays," in *Proc. European Radar Conference (EuRAD)*, (Paris, France), Sept. 2015.

[11] D. Bleh and *et al.*, "W-band time-domain multiplexing FMCW MIMO radar for far-field 3-D imaging," *IEEE Trans. Microw. Theory Tech.*, vol. 65, no. 9, pp. 3474–3484, 2017.

[12] J. Bechter, F. Roos, and C. Waldschmidt, "Compensation of motion-induced phase errors in TDM MIMO radars," *IEEE Microw. Wireless Compon. Lett.*, vol. 27, no. 12, pp. 1164–1166, 2017.

[13] F. Jansen, A. Filippi, and Z. Zivkoic, "MIMO radar system," (European Patent EP3021132A1), May 18, 2016.

[14] F. Roos, J. Bechter, N. Appenrodt, J. Dickmann, and C. Waldschmidt, "Enhancement of Doppler unambiguity for chirp-sequence modulated TDM-MIMO radars," in *Proc. Intl. Conference on Microwaves for Intelligent Mobility (ICMIM)*, (Munich, Germany), April 2018.

[15] V. F. Mecca, D. Ramakrishnan, and J. L. Krolik, "MIMO radar space-time adaptive processing for multipath clutter mitigation," in *Proc. IEEE Workshop on Sensor Array and Multichannel Processing (SAM)*, (Waltham, MA), July 2006.

[16] H. Sun, F. Brigui, and M. Lesturgie, "Analysis and comparison of MIMO radar waveforms," in *Proc. Intl. Radar Conference*, (Lille, France), Oct. 2014.

[17] N. Madsen and S. Cao, "Slow-time waveform design for MIMO GMTI radar using CAZAC sequences," in *Proc. IEEE Radar Conference*, (Oklahoma City, OK), April 2018.

[18] J. Benedetto, I. Konstantinidis, and M. Rangaswamy, "Phase-coded waveforms and their design," *IEEE Signal Process. Mag.*, vol. 26, no. 1, pp. 22–31, 2009.

[19] D. Chu, "Polyphase codes with good periodic correlation properties," *IEEE Trans. Inf. Theory*, vol. 18, no. 4, pp. 531–532, 1972.

[20] R. Feger, H. Haderer, and A. Stelzer, "Optimization of codes and weighting functions for binary phase-coded FMCW MIMO radars," in *Proc. Intl. Conference on Microwaves for Intelligent Mobility (ICMIM)*, (San Diego, CA), May 2016.

[21] R. Feger, C. Pfeffer, and A. Stelzer, "A frequency-division MIMO FMCW radar system based on Delta-Sigma modulated transmitters," *IEEE Trans. Microw. Theory Tech.*, vol. 62, no. 12, pp. 3572–3581, 2014.

[22] P. Hacker and B. Yang, "Single snapshot DOA estimation," *Advances in Radio Science*, vol. 8, pp. 251–256, 2010.

[23] P. Barton, "Digital beam forming for radar," *IEE Proceedings F - Communications, Radar and Signal Processing*, vol. 127, no. 4, 1980.

[24] S. Alland and J. Searcy, "Radar system and method of digital beamforming," (U.S. Patent 2009/0085800), April 2, 2009.

[25] S. Tokoro, K. Kuroda, A. Kawakubo, K. Fujita, and H. Fujinami, "Electronically scanned millimiter-wave radar for precrash safety and adaptive cruise control system," in *Proc. IEEE Intelligent Vehicles Symposium*, (Columbus, OH), June 2003.

[26] R. Schmidt, "Multiple emitter location and signal parameter estimation," *IEEE Trans. Antennas Propag.*, vol. 34, no. 3, pp. 276–280, 1986.

[27] R. Roy and T. Kailath, "ESPRIT - estimation of signal parameters via rotation invariance techniques," *IEEE Trans. Acoust., Speech, Signal Process.*, vol. 17, no. 7, pp. 984–995, 1989.

[28] G. Xu, S. D. Silverstein, R. H. Roy, and T. Kailath, "Beamspace ESPRIT," *IEEE Trans. Signal Process.*, vol. 42, no. 2, pp. 349–356, 1994.

[29] M. Haardt and J. Nossek, "Unitary ESPRIT: How to obtain increased estimation accuracy with a reduced computational burden," *IEEE Trans. Signal Process.*, vol. 43, no. 5, pp. 1232–1242, 1995.

[30] M. D. Zoltowski, M. Haardt, and C. Mathews, "Closed-form 2-D angle estimation with rectangular arrays in element space or beamspace via unitary ESPRIT," *IEEE Trans. Signal Process.*, vol. 44, no. 2, pp. 316–328, 1996.

[31] T. Strohmer and B. Friedlander, "Compressed sensing for MIMO radar - algorithms and performance," in *Proc. 43th Annual Asilomar Conference on Signals, Systems, and Computers*, (Pacific Grove, CA), Nov. 2009.

[32] Y. Yu, A. P. Petropulu, and H. V. Poor, "MIMO radar using compressive sampling," *IEEE J. Sel. Topics Signal Process.*, vol. 4, no. 1, pp. 146–163, 2010.

[33] Y. Yu, A. P. Petropulu, and H. V. Poor, "Measurement matrix design for compressive sensing-based MIMO radar," *IEEE Trans. Signal Process.*, vol. 59, no. 11, pp. 5338–5352, 2011.

[34] Y. Yu, A. P. Petropulu, and H. V. Poor, "CSSF MIMO radar: Compressive-sensing and step-frequency based MIMO radar," *IEEE Trans. Aerosp. Electron. Syst.*, vol. 48, no. 2, pp. 1490–1504, 2012.

[35] Y. Yu, S. Sun, R. N. Madan, and A. P. Petropulu, "Power allocation and waveform design for the compressive sensing based MIMO radar," *IEEE Trans. Aerosp. Electron. Syst.*, vol. 50, no. 2, pp. 898–909, 2014.

[36] T. Strohmer and B. Friedlander, "Analysis of sparse MIMO radar," *Appl. Comp. Harm. Anal.*, vol. 37, pp. 361–388, 2014.

[37] S. Sun, "MIMO Radars with Sparse Sensing," Ph.D. Dissertation, Rutgers University, New Brunswick, NJ, 2016.

[38] S. Sun, W. U. Bajwa, and A. P. Petropulu, "MIMO-MC radar: A MIMO radar approach based on matrix completion," *IEEE Trans. Aerosp. Electron. Syst.*, vol. 51, no. 3, pp. 1839–1852, 2015.

[39] S. Sun and A. P. Petropulu, "Waveform design for MIMO radars with matrix completion," *IEEE J. Sel. Topics Signal Process.*, vol. 9, no. 8, pp. 1400–1411, 2015.

[40] T. Yardibi, J. Li, P. Stoica, M. Xue, and A. Baggeroer, "Source localization and sensing: A nonparametric iterative adaptive approach based on weighted least squares," *IEEE Trans. Aerosp. Electron. Syst.*, vol. 46, no. 1, pp. 425–443, 2010.

[41] W. Roberts, P. Stoica, J. Li, T. Yardibi, and F. Sadjadi, "Iterative adaptive approaches to MIMO radar imaging," *IEEE J. Sel. Topics Signal Process.*, vol. 4, no. 1, pp. 5–20, 2010.

[42] T. Shan, M. Wax, and T. Kailath, "On spatial smoothing for direction-of-arrival estimation of coherent signals," *IEEE Trans. Acoust., Speech, Signal Process.*, vol. 33, no. 4, pp. 506–811, 1985.

[43] M. A. Richards, *Fundamentals of Radar Signal Processing, 2nd Ed.* New York, McGraw-Hill, 2014.

[44] L. Carin, D. Liu, and B. Guo, "Coherence, compressive sensing, and random sensor arrays," *IEEE Antennas Propag. Mag.*, vol. 53, no. 4, pp. 28–39, 2011.

[45] C. Schmid, R. Feger, C. Wagner, and A. Stelzer, "Design of a linear non-uniform antenna array for a 77-GHz MIMO FMCW radar," in *Proc. IEEE MTT-S Intl. Microwave Workshop on Wireless Sensing, Local Positioning, and RFID*, (Cavtat, Croatia), Sept. 2009.

[46] C. A. Alcalde, "Radar system and method for virtual antenna signals," (U.S. Patent 9 664 775 B2), May 30, 2017.

[47] Z. Li and C. A. Alcalde, "Angle finding for a detector having a paired staggered array," (U.S. Patent 2018/0267555 A1), Sept. 20, 2018.

[48] S. Alland, "MIMO antenna with improved grating lobe characteristics," (U.S. Patent 2015/0253419 A1), Sept. 10, 2015.

[49] J. Searcy and S. Alland, "MIMO antenna with elevation detection," (U.S. Patent 9 541 639 B2), Jan. 10, 2017.

[50] H. Akaike, "A new look at the statistical model identification," *IEEE Trans. Acoust., Speech, Signal Process.*, vol. 37, no. 1, pp. 8–15, 1989.

[51] Y. Barron, J. Rissanen, and B. Yu, "The minimum description length principle in coding and modeling," *IEEE Trans. Inf. Theory*, vol. 44, no. 6, pp. 2743–2760, 1998.

[52] S. U. Pillai and B. H. Kwon, "Forward/backward spatial smoothing techniques for coherent signal identification," *IEEE Trans. Acoust., Speech, Signal Process.*, vol. 37, no. 1, pp. 8–15, 1989.

[53] A. E. Ertan and M. Ali, "Spatial and temporal smoothing for covariance estimation in super-resolution angle estimation in automotive radars," in *Proc. IEEE Int. Conf. Acoust., Speech, Signal Process. (ICASSP)*, (Barcelona, Spain), May 4-8, 2020.

[54] E. J. Candès and J. Romberg, "Sparsity and incoherence in compressive sampling," *Inverse Problems*, vol. 23, pp. 969–985, 2007.

[55] E. J. Candès and T. Tao, "The Dantzig selector: Statistical estimation when p is much larger than n," *The Annals of Statistics*, vol. 35, no. 6, pp. 2313–2351, 2007.

[56] T. T. Cai and L. Wang, "Orthogonal matching pursuit for sparse signal recovery with noise," *IEEE Trans. Inf. Theory*, vol. 57, no. 7, pp. 4680–4688, 2011.

[57] G. Tang, B. N. Bhaskar, P. Shah, and B. Recht, "Compressed sensing off the grid," *IEEE Trans. Inf. Theory*, vol. 59, no. 11, pp. 7465–7490, 2013.

[58] Y. Chi, L. L. Scharf, A. Pezeshki, and A. R. Calderbank, "Sensitivity to basis mismatch in compressed sensing," *IEEE Trans. Signal Process.*, vol. 59, no. 5, pp. 2182–2195, 2011.

[59] Y. T. Lo, "A mathematical theory of antenna arrays with randomly spaced elements," *IEEE Trans. Antennas Propag.*, vol. 12, no. 3, pp. 257–268, 1964.

[60] S. Alland and *et al.*, "Virtual radar configuration for 2D array," (U.S. Patent 9 869 762), Jan. 16, 2018.

[61] T. Spreng and *et al.*, "Wideband 120 GHz to 140 GHz MIMO radar: System design and imaging results," in *Proc. European Microwave Conference (EuMC)*, (Paris, France), Sept. 2015.

[62] F. Meinl, M. Stolz, M. Kunert, and H. Blume, "An experimental high performance radar system for highly automated driving," in *Proc. Intl. Conference on Microwaves for Intelligent Mobility (ICMIM)*, (Nagoya, Japan), Mar. 2017.

[63] J. Ying, J. F. Cai, D. Guo, G. Tang, Z. Chen, and X. Qu, "Vandermonde factorization of Hankel matrix for complex exponential signal recovery-application in fast NMR spectroscopy," *IEEE Trans. Signal Process.*, vol. 66, no. 21, pp. 5520–5533, 2018.

[64] E. J. Candès and B. Recht, "Exact matrix completion via convex optimization," *Foundations of Computational Mathematics*, vol. 9, no. 6, pp. 717–772, 2009.

[65] J. F. Cai, E. J. Candès, and Z. Shen, "A singular value thresholding algorithm for matrix completion," *SIAM J. Optim.*, vol. 20, no. 2, pp. 1956–1982, 2010.

[66] Velodyne, "HDL-32E high definition real-time LiDAR," datasheet, [Available Online] https://velodynelidar.com/products/hdl-32e/, 2021.

[67] Y. Hua, "Estimating two-dimensional frequencies by matrix enhancement and matrix pencil," *IEEE Trans. Signal Process.*, vol. 40, no. 9, pp. 2267–2280, 1992.

[68] M. Grant and S. Boyd, "CVX: Matlab software for disciplined convex programming, version 2.1." http://cvxr.com/cvx, Mar. 2014.

[69] M. Rossi, A. Haimovich, and Y. Eldar, "Spatial compressive sensing for MIMO radar," *IEEE Trans. Signal Process.*, vol. 62, no. 2, pp. 419–430, 2014.

[70] R. Feger, C. Wagner, S. Schuster, S. Scheiblhofer, H. Jager, and A. Stelzer, "A 77-GHz FMCW MIMO radar based on an SiGe single chip transceiver," *IEEE Trans. Microw. Theory Tech.*, vol. 57, no. 5, pp. 1020–1035, 2009.

[71] N. Jin and Y. Rahmat-Samii, "Advances in particle swarm optimization for antenna designs: Real-number, binary, single-objective and multiobjective implementations," *IEEE Trans. Antennas Propag.*, vol. 55, no. 3, pp. 556–567, 2007.

[72] M. Gonalez-Huici, D. Mateos-Nunez, C. Greiff, and R. Simoni, "Constrained optimal design of automotive radar arrays using the Weiss-Weinstein bound," in *Proc. Intl. Conference on Microwaves for Intelligent Mobility (ICMIM)*, (Munich, Germany), April 2018.

[73] I. Bilik and *et al.*, "Automotive multi-mode cascaded radar data processing embedded system," in *Proc. IEEE Radar Conference*, (Oklahoma City, OK), April 2018.

[74] A. Och, C. Pfeffer, J. Schrattenecker, S. Schuster, and R. Weigel, "A scalable 77 GHz massive MIMO FMCW radar by cascading fully-integrated transceivers," in *Proc. Asia-Pacific Microwave Conference (APMC)*, (Kyoto, Japan), Nov. 6-9, 2018.

[75] https://www.zf.com/products/en/cars/products_58368.html, May 2021.

[76] https://www.continental-automotive.com, May 2021.

[77] Texas Instruments Inc., "Design guide: TIDEP-01012 imaging radar using cascaded mmWave sensor reference design (REV. A)," [Available Online] https://www.ti.com/lit/ug/tiduen5a/tiduen5a.pdf, Mar., 2020.

[78] A. Moffet, "Minimum-redundancy linear arrays," *IEEE Trans. Antennas Propag.*, vol. 16, no. 2, pp. 172–175, 1968.

[79] V. Giannini and *et al.*, "A 192-virtual-receiver 77/79GHz GMSK code-domain MIMO radar system-on-chip," in *Proc. IEEE Intl. Solid-State Circuits Conference (ISSCC)*, (San Francisco, CA), Feb. 17-21, 2019.

[80] (https://vayyar.com/).

[81] A. Ioffe, W. Doerr, H. Yan, D. H. Vu, and A. H. Arage, "RCS characteristics of street curbs and the applications in automotive radar classification," in *Proc. European Radar Conference (EuRAD)*, (London, UK), Oct. 2016.

[82] F. Engels, M. Wintermantel, and P. Heidenreich, "Automotive MIMO radar angle estimation in the presence of multipath," in *Proc. European Radar Conference (EuRAD)*, (Nuremberg, Germany), Oct. 2017.

[83] T. Visentin, J. Hasch, and T. Zwick, "Analysis of multipath and DOA detection using a fully polarimetric automotive radar," in *Proc. European Radar Conference (EuRAD)*, (Nuremberg, Germany), Oct. 2017.

[84] L. B. Fertig, J. M. Baden, and J. R. Guerci, "Knowledge-aided processing for multipath exploitation radar (MER)," *IEEE Aerosp. Electron. Syst. Mag.*, vol. 32, no. 10, pp. 24–36, 2017.

[85] W. V. Thillo and *et al.*, "Almost perfect auto-correlation sequences for binary phase-modulated continuous wave radar," in *Proc. European Radar Conference (EuRAD)*, (Nuremberg, Germany), Oct. 2013.

[86] V. Giannini and *et al.*, "A 79 GHz phase-modulated 4 GHz-BW CW radar transmitter in 28 nm CMOS," *IEEE J. Solid-State Circuits*, vol. 49, no. 12, pp. 2925–2937, 2014.

[87] A. Bourdoux, U. Ahmad, D. Guermandi, S. Brebels, A. Dewilde, and W. V. Thillo, "PMCW waveform and MIMO technique for a 79 GHz CMOS automotive radar," in *Proc. IEEE Radar Conference*, (Philadelphia, PA), May 2016.

[88] D. Guermandi and *et al.*, "A 79-GHz 2x2 MIMO PMCW radar SoC in 28-nm CMOS," *IEEE J. Solid-State Circuits*, vol. 52, no. 10, pp. 2613–2626, 2017.

[89] L. Welch, "Lower bounds on the maximum cross correlation of signals (corresp.)," *IEEE Trans. Inf. Theory*, vol. 20, no. 3, pp. 397–399, 1974.

[90] R. Gold, "Optimal binary sequences for spread spectrum multiplexing (corresp.)," *IEEE Trans. Inf. Theory*, vol. 13, no. 4, pp. 619–621, 1967.

[91] T. Kasami, "Weight distribution formula for some class of cyclic codes," *Report*, pp. 1–32, 1966.

[92] E. H. Dinan and B. Jabbari, "Spreading codes for direct sequence CDMA and wideband CDMA cellular networks," *IEEE Commun. Mag.*, vol. 36, no. 9, pp. 48–54, 1998.

[93] G. Hueber and A. M. Niknejad, *Millimeter-Wave Circuits for 5G and Radar*. Cambridge University Press, Cambridge, UK, 2019.

[94] F. Liu, C. Masouros, A. P. Petropulu, H. Griffiths, and L. Hanzo, "Joint radar and communication design: Applications, state-of-the-art, and the road ahead," *IEEE Trans. Commun.*, to appear.

[95] W. V. Thillo, V. Giannini, D. Guermandi, S. Brebels, and A. Bourdoux, "Impact of ADC clipping and quantization on phase-modulated 79 GHz CMOS radar," in *Proc. European Radar Conference (EuRAD)*, (Rome, Italy), Oct. 2014.

[96] H. Rohling and M.-M. Meinecke, "Waveform design principles for automotive radar systems," in *Proc. CIE Intl. Conference on Radar*, (Beijing, China), Oct. 2001.

[97] M. Xue, L. Xu, and J. Li, "IAA spectral estimation: Fast implementation using the Gohberg-Semencul factorization," *IEEE Trans. Signal Process.*, vol. 59, no. 7, pp. 3251–3261, 2011.

[98] G. O. Glentis and A. Jakobsson, "Efficient implementation of iterative adaptive approach spectral estimation techniques," *IEEE Trans. Signal Process.*, vol. 59, no. 9, pp. 4154–4167, 2011.

[99] G. O. Glentis and A. Jakobsson, "Superfast approximative implementation of the IAA spectral estimate," *IEEE Trans. Signal Process.*, vol. 60, no. 1, pp. 472–478, 2012.

[100] L. C. Godara, "Application of antenna arrays to mobile communications. II. Beam-forming and direction-of-arrival considerations," *Proceedings of the IEEE*, vol. 85, no. 8, pp. 1195–1245, 1997.